DIPLOMARBEIT

DEVELOPMENT AND IMPROVEMENT OF X-RAY SPECTROSCOPIC TECHNIQUES FOR IONIC LIQUIDS

Institute of Atomic and Subatomic Physics
Vienna University of Technology

under supervision of

Univ.Ass. Dipl.-Phys. Dr.rer.nat. Yuji Hasegawa and

Univ.Prof. Dipl.-Phys. Dr.rer.nat. Yoshihisa Harada

by

Roman Zöchling

August 31, 2018

Contents

Kurzfassung

Eine der heute am meisten verwendeten und damit eine der wichtigsten Technologien stellt der Lithium-Ionen-Akku dar. Er befindet sich in so gut wie jedem elektronischen Geraet, das wir mit uns fuehren - sei es ein Laptop, ein Tablet, ein e-Reader, oder - vor allem - unser Mobiltelefon, das man schon fast als unser zweites bzw. Ersatzhirn bezeichnen koennte. Zu diesem Akku gibt es hinsichtlich Leistung, Gewicht, und nicht zuletzt dem Preis-Leistungsverhaeltnis kaum eine Alternative. Es wird zwar regelmaessig an neuen Akku-Technologien geforscht und ab und an von einem Durchbruch berichtet, aber bisher ist es noch nicht gelungen, den Li-Ionen-Akku durch eine bessere Technologie zu ersetzen.

In juengerer Zeit ist es zu mehreren Unfaellen gekommen, bei denen Akkus zu heiss wurden und schlussendlich explodiert sind. Dies ist vor allem darauf zurueckzufuehren, dass Hersteller versuchen, moeglichst viel Akkuleistung in ein moeglichst kleines Gehaeuse zu pressen - was einerseits verstaendlich ist, andererseits aber, wenn dabei nicht sorgfaeltig genug vorgegangen wird, zu den genannten Unfaellen fuehren kann. Das bedeutet, dass man als Nutzer auf die Sorgfaltspflicht der Hersteller vertrauen muss.

Um diese Situation zu verbessern, wird seit einiger Zeit an sogenannten waessrigen oder wasserhaltigen Li-Ionen-Batterien geforscht, die eine sichere Nutzung versprechen. Bisher lagen diese Batterien in Sachen Leistungsfaehigkeit und maximale Kapazitaet aber weit hinter den herkoemmlichen zurueck. Mit dem Aufkommen von Fluessigsalzen (hydrate melts) - Salze, die sich bei Zugabe von wenig Wasser darin aufloesen - hat sich die Leistung dieser Fluessigbatterien um Groessenordnungen verbessert und dringt in den Bereich vor, der heute von festen Li-Ionen-Akkus erfuellt wird.

In dieser Diplomarbeit soll vor allem die Struktur dieser Fluessigsalze mithilfe von Roentgenspektroskopie erforscht werden, um einen Konnex zwischen innerer Struktur der Fluessigkeit und makroskopischen Eigenschaften herzustellen. Dazu wurden sowohl Roentgenabsorptions- als auch -emissionsspektren verschiedener Fluessigsalz-Mischungen angefertigt und gleichzeitig theoretische Simulationen der Struktur dieser Salze durchgefuehrt, um die Gestalt dieser Spektren zu erklaeren.

In einem weiteren Schritt wurden Ray-Tracing-Simulationen durchgefuehrt, um die Spezifikationen fuer die optischen Elemente eines neuen bzw. eines ueberarbeiteten Emissionsspektrometers herauszufinden. Dabei galt es, mehrere Vorgaben wie etwa die maximale Laenge des Spektrometers oder eine gewisse minimale Akzeptanz einzuhalten. Diese Berechnungen dienen dem Konzept dieser Spektrometer fuer eine neue Beamline an einem zukuenftigen Synchrotron in Japan. Das Ziel dabei ist eine deutliche Erhoehung der Aufloesung um einen Faktor von mindestens 10. Damit werden ganz neue Moeglichkeiten der Roentgenspektroskopie realisiert werden, die zu neuen Einsichten betreffend einer Vielzahl von Materialien fuehren wird, darunter auch im Bereich der wasserhaltigen

Batterien.

Abstract

One of the most important and most widely used technologies in everyday life is the Lithium-ion battery. This battery is implemented in almost every portable device - be it a laptop, a tablet, an e-Reader or - above all - a mobile phone, which could be called our second or substitute brain. There is no real alternative to this battery taking into account performance, weight and value for money. All the time there is indeed research being conducted on new battery technologies and every now and then there appears an article about a breakthrough in a new and innovative battery technology, but until now, nobody was able to introduce a new technology capable of surpassing the Li-ion battery.

Recently, several cases of battery overheating and consequent explosion were reported and became publicly known. This is a consequence of the manufacturer's desire to implement as much battery performance as possible in a case as small as possible - on the one hand, this desire is reasonable, but on the other hand, if handled carelessly, can lead to the above mentioned accidents. This essentially means that the customer is dependent on the manufacturer's obligation to exercise due care.

To get out of this dilemma, the utilisation of aqueous batteries was studied for quite a long time. Until recently, the performance and maximum capacity of these batteries were far behind commonly used solid Li-ion batteries. With the emergence of hydrate melts at room temperature, i.e. salts, that are dissolved with the addition of a small amount of water, the performance of these aqueous batteries increased dramatically and is reaching now levels comparable to those of solid Li-ion batteries.

In this thesis, the structure of these hydrate melts is discussed by applying X-ray emission and absorption spectroscopy, respectively, to investigate the connection between inner structure and macroscopic properties. To achieve this, we analysed the experimental spectra of several hydrate melt solutions and at the same time performed theoretical DFT calculations and MD simulations to see, if we can reproduce the experimental spectra with simplified theoretical models.

In the next step, the properties of several optical elements that will be used at a new ultra-high resolution spectrometer and an updated spectrometer, respectively, were calculated using the ray-tracing code SHADOW. They are part of the conceptual phase for a new beamline at a future synchrotron in Japan, scheduled for construction in 2019. The goal is to significantly increase the reachable energy resolution by a factor of at least 10, surpassing the capability of any other instrument in Japan. If this goal is met, entirely new possiblities of X-ray spectroscopy will be realised, which in turn will open the doors towards the understanding of a wide range of materials, among which also aqueous batteries reside.

1   Motivation

Ionic liquids or molten salts are salts in the liquid state. As the name is already suggesting, ionic liquids consist largely of ions and short-lived ion pairs, whereas ordinary liquids such as water are predominantly made of electrically neutral molecules. This gives them unusual physical properties, such as high electric conductivity high solvation power, making them interesting candidates for aqueous electrolytes in batteries. Hydrate melts, metal salts dissolved in an extremely small amount of water, where all the H_2O molecules are coordinated with the metal cations [16] while retaining their fluidity, are a class of these ionic liquids. They possess properties analogous to those of classical molten salts. Until recently, hydrate melts were only available either at high temperatures or high pressure, reducing their potential as industrial applications. However, in 2016, the Yamada group at the University of Tokyo found a hydrate melt at room temperature [3], and demonstrated its application as an electrolyte in an aqueous lithium-ion battery.

A lithium-ion battery (LIB) is a type of rechargable battery where lithium ions act as the charge carriers between the two electrodes of the battery. They move from the negative electrode (anode) through the electrolyte to the positive electrode (cathode). One of the electrodes is made of an intercalated lithium compound, giving the lithium-ion battery its name.

Since the emergence of LIBs in the 1990s, they have almost entirely conquered the market of batteries for consumer electronics and portable electrical appliances. Raised concerns of safety issues, such as the possibility of explosions due to overheating or malfunction of the battery, or the harmful effects to the environment leakage of the toxic components of these batteries could cause, were outweighed by high energy and power densities, negligible self-discharge, low weight and low production cost.

However, various types of LIBs using different kinds of electrode materials exist, typically counterbalancing high performance with high reliability and long lifetime. Growing in popularity as applications in electric vehicles, in the military or in aerospace, there is an increased demand in improving the stability and longevity at the cost of performance, which is still higher as in comparable types of batteries.

As a prospective candidate to fulfil these demands, LIBs using an aqueous electrolyte have been proposed already in the 1990s [1]. While the typical LIB is non-aqueous, and relies on an organic electrolyte as that allows for ionic movement between the two electrodes, in the case of aqueous batteries an aqueous mixture takes the role of the electrolyte. This comes at the expense of capacity and performance, but greatly reduces the environmental impact due to not using any toxic materials, and the risk of explosion by using a non-flammable electrolyte.

The voltage and charge stored in an electrochemical cell are determined by the chemistry of the electrodes. The limitation of aqueous batteries comes from the fact that a viable battery can only
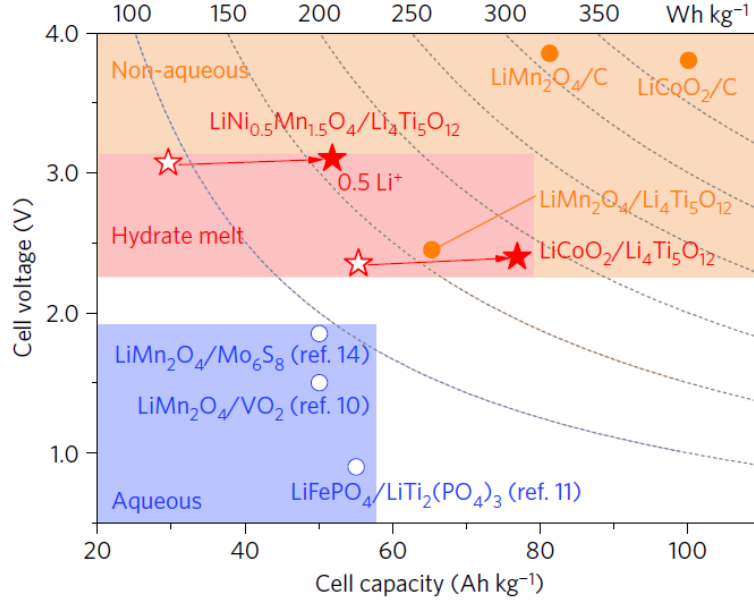
Figure 1: Overview of different types of Li-ion batteries using an aqueous (blue), hydrate melt (red), or non-aqueous (orange) electrolyte. Filled stars and circles represent theoretical values, while open stars and circles represent actual values. Hydrate melt electrolytes are able to bridge the gap between aqueous and non-aqueous batteries. Taken from [3].

be constructed if the electrolyte remains stable against the electrodes over the voltage range. Since the onset of water electrolysis is at $1.23\,\text{eV}$, this sets the limits for the electrochemical potential window.

However, there have been several attempts to increase this potential window. One of the most successful approaches is the use of a "water-in-salt" or hydrate melt electrolytes, as demonstrated in [2] or [3]. Using these electrolytes enables the formation of solid-electrolyte interphase (SEI) layers at the surface of the electrodes, protecting them from the evolution of H_2 and O_2 at the electrodes and thus greatly increasing the stability window to $3\,\text{eV}$ and above.

Fig. 1 shows a comparison of the available types of LIBs using aqueous, hydrate melt and non-aqueous electrolytes. With the application of hydrate melts, the capacity and the available potential window of aqueous batteries greatly increases and thus enables high-energy-density aqueous batteries comparable to certain types of solid-state LIBs.

As such, hydrate melt electrolytes might pave the way for future aqueous LIB applications combining the high performance of organic electrolyte batteries with the reliability and longevity of aqueous batteries. Of particular interest is the electronic and geometrical structure of these hydrate melt solutions and the hydrogen bonding network the lithium salts form together with
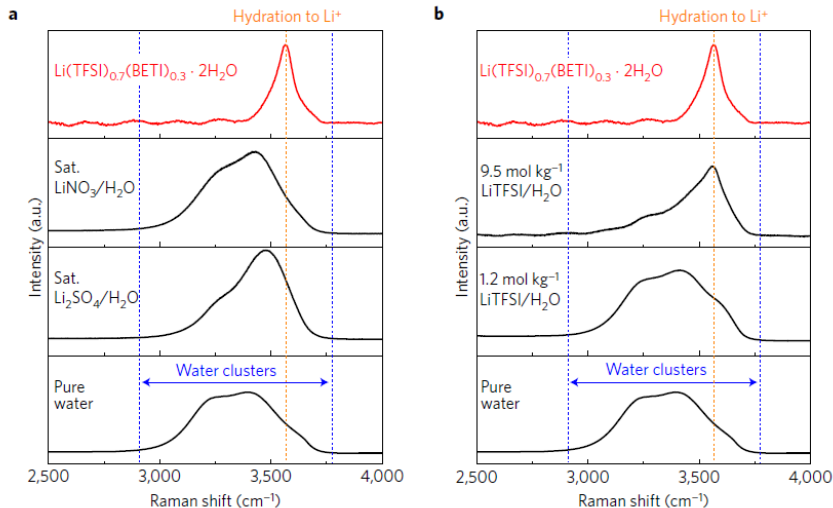
Figure 2: Raman spectra of hydrate melt (red) compared to those of inorganic Li salt aqueous solutions. O-H stretching modes of water molecules are typically observed in the range of $2500 \frac{1}{\text{cm}}$ - $4000 \frac{1}{\text{cm}}$ of the Raman bands. While the hydrate melt spectrum exhibits a sharp peak at $3565 \frac{1}{\text{cm}}$, interpreted as H_2O molecules coordinated with Li^+ cations that are not clustered through hydrogen bonding, the broad bands observed in the other spectra are attributed to the hydrogen bond network of clustered water molecules. Taken from [3].

H_2O. Knowledge of the inherent structure leads to a better understanding of the physical and electrochemical properties of the hydrate melts and thus is important for the further improvement and development of electrolytes for high-energy-density aqueous batteries.

The scope of this work consists of two main points. First, as part of the Yamada group hydrate melt collaboration, we want to further investigate the geometric and electronic structure of the hydrate melt presented in their paper, and foster the already obtained knowledge and assumptions by means of soft X-ray spectroscopy.

While the study of hydrate melt already includes X-ray Raman spectroscopy of several hydrate melt samples (Fig. 2, which shows the assumed hydration of H_2O to Li^+ by exhibiting a sharp peak in the Raman spectrum as the salt concentration increases, the conclusions about the structure from these results are a only an assumption.

For a more precise determination of the $Li-H_2O$ interaction and its local environment, we chose to employ both soft X-ray abssorption and emission spectroscopy (XAS and XES, respectively) to probe the unoccupied as well as the occupied density of states. These give a clear picture about the electronic structure below and above the Fermi level and help to better understand what gives the hydrate melt its unusual physical and electrochemical properties. As this was previously unknown, we found some intriguing results in the obtained spectra.

However, in combination with these experiments, and encouraged by previous calculations of liquid systems as for example in [17], we also strived to tackle the problem from the theoretical viewpoint. By modeling the clusters of the hydrate melt in question and simulating ab initio molecular dynamics of these clusters, we wanted to cut out small localised structures from the clusters and use them as model geometries for theoretical calculations of XAS and XES spectra. Even though our model is quite simple, interesting conclusions can be drawn by using this approach.

From the results of this analysis, we arrived at a level where we could not get a deeper understanding using the above mentioned spectroscopic techniques, and concluded that only by improving the resolution we would be able to obtain XAS, XES and RIXS (Resonant Inelastic X-ray spectra) spectra with higher significance for our issue. Looking for ways to improve the spectrometer used for our experiments, ray-tracing calculations for the optical elements and the spectrometer geometry were carried out, and the upgrade using these calculations as a basis will significantly improve the resolving power.

2 Background

2.1 The soft X-ray region of the electromagnetic spectrum

Up to these days, the X-ray region of the electromagnetic spectrum remains one of the least developed. This is due to the fact that the corresponding wavelengths, from several nm to the sub-nano regime, are comparatively short. Lacking the necessary equipment, it has proven difficult to explore this region in the past. Nowadays, with more and more sophisticated optics and detectors with ever higher resolution becoming available, the X-ray region of the electromagnetical spectrum becomes ever more accessible.
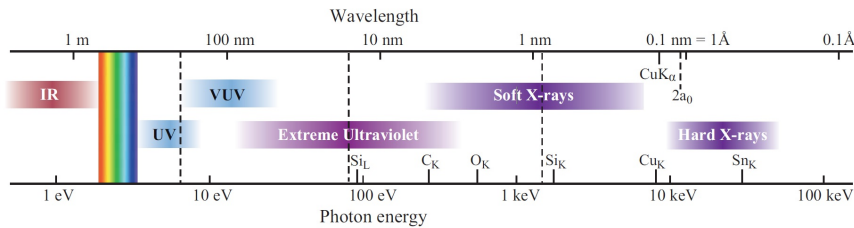

Figure 3: The electromagnetic spectrum, extending from the infrared to X-ray regions. Corresponding wavelengths and energies are shown at the top and the bottom range, respectively. Soft X-rays are photons with an energy from 250 eV up to several keV. For better orientation, absorption edges of several elements are included in the sketch. The O K-edge, which is of particular interest in research of water and water-related liquids, is located at 543 eV. Taken from [4]).

When talking about soft X-rays, since the term 'soft' is not entirely precise, first the corresponding energy range has to be defined. Following Attwood and Sakdinawat [4], here the soft X-ray region is the region of the electromagnetic spectrum ranging from 250 eV up to several keV (Fig. 3). Using the energy-to-wavelength conversion,

$$hc = 1239.841 \, \text{eV} \cdot \text{nm}, \tag{1}$$

the corresponding wavelength is ranging from 5 nm to < 1 nm. The soft X-ray region is of particular interest for conducting experiments with biological or chemical samples with low-Z elements, such as C, N or O, since their primary atomic excitations, the removal of a core electron from the most tightly bound orbitals (K-edge absorption), lie exactly in this region. This energy also corresponds to the excitation energy of collective phenomena like magnons, spinons etc. in many-body compound systems and is therefore suitable for investigation of complex d- and f-materials. Our lab's main research topic is the structure of water and of any materials related to water - and as such, soft X-ray spectroscopy is the tool of choice for investigation of these liquids, above all, because it is very sensitive to structural changes in the material. When probing aqueous
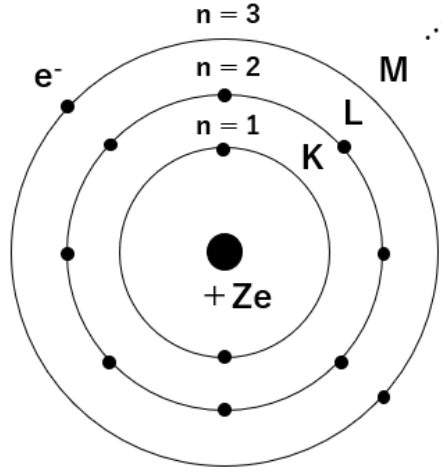
Figure 4: Bohr model of the atom, depicting electrons with charge $-e$ circulating on defined orbits around the nucleus with charge $+Ze$. The orbits are called shells, and, depending on the principal quantum number n associated with the shell, are called K-shell, L-shell, M-shell and so forth.

compounds, usually the O K-Edge at $543\,\mathrm{eV}$ is of utmost interest, its energy however can change slightly depending on the chemical environment of the oxygen.

Typical experimental methods for the analysis of above mentioned materials include X-ray Absorption Near Edge Spectroscopy (XANES) and Extended X-ray Absorption Fine Structure (EXAFS), Resonant Inelastic X-ray Scattering (RIXS), X-ray Photoelectron Spectroscopy (XPS), and many more. The most relevant for this thesis are described in the following section.

2.2   Atomic Energy Levels and Allowed Transitions

Niels Bohr was the first to introduce a model of the atom, where the electrons move on clearly defined circular orbits around the nucleus, which later became known as the Bohr model. Even if this model was presented before the advent of quantum mechanics and now more accurate descriptions of atoms are available, the Bohr model is still applicable in many cases, where it suffices to explain many basic phenomena related with atomic transitions.

Fig. 4 shows a sketch of the Bohr model. Electrons with charge $-e$ are located in shells with well-defined energies and radii around a small nucleus with positive charge $+Ze$. By equating the coulomb force $Ze^2/4\pi\epsilon_0 r^2$ of the nucleus and the centripetal force mv^2/r under the condition of quantized angular momentum $mvr = n\hbar$ ($n = 1, 2, 3, ...$), Bohr obtained stationary electron orbits with energy E_n and radius r_n,

$$E_n = -\frac{mZ^2 e^4}{32\pi^2 \epsilon_0^2 \hbar^2} \frac{1}{n^2} \tag{2}$$

and

$$r_n = \frac{4\pi\epsilon_0 \hbar^2}{mZe^2} \cdot n^2 \tag{3}$$

where m and e correspond to electron mass and charge, Ze to the nuclear charge, ϵ_0 to the vacuum permittivity, and $\hbar$ to Planck's constant h divided by 2π.

Transitions in the Bohr model are only allowed between the stationary electron orbits, leading to characteristic emission of photons of energy

$$\hbar\omega = E_i - E_f = \frac{mZ^2 e^4}{32\pi^2 \epsilon_0^2 \hbar^2} \left(\frac{1}{n_f^2} - \frac{1}{n_i^2} \right) \tag{4}$$

for transitions from shell i to shell j. These emission lines are characteristic for particular elements, since they involve the element-specific proton number Z and the number of transitions is resctricted to the possible combinations of n_i and n_f.

With the Bohr model, it became possible to explain optical spectra of hydrogen (Balmer series), with $n_f = 2$ and $n_i = 3, 4, 5, ...$, the Lyman series with $n_f = 1$ and $n_i = 2, 3, 4, 5, ...$, etc. However, not all of the emission lines among the possible quantum states predicted by the model were observed, suggesting that some transitions are not allowed while others are, and the model itself stood in conflict with classical radiation physics in that for the Bohr model to work, the electrons would have had to be continuously accelerated, while not emitting radiation and losing energy on their circular orbit.

These contridactions led to the development of modern quantum mechanics based on wave mechanics, where the particle's motion is described by a wave function $\Psi(\vec{r}, t)$, obeying the equation

$$\left[-\frac{\hbar^2}{2m} \boldsymbol{\nabla}^2 + V(\vec{r}, t) \right] \Psi(\vec{r}, t) = i\hbar \frac{\partial \Psi(\vec{r}, t)}{\partial t}, \tag{5}$$

Eq. 5 is known as Schroedinger's equation.

Bremsstrahlung and characteristic X-ray emission

Selection rules

$$\Delta n \neq 0 \tag{6}$$

$$\Delta l = \pm 1 \tag{7}$$

$$\Delta j = 0, \pm 1 \tag{8}$$

$$\Delta m_l = 0, \pm 1 \tag{9}$$

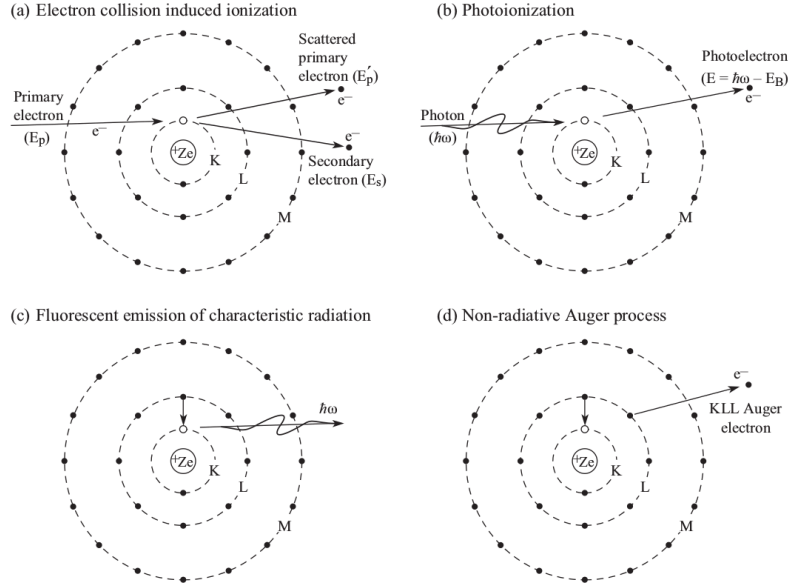### 2.2.1 Interaction of photons with matter

Figure 5: Basic emission and absorption processes of photons interacting with matter: ionisation induced by electron collision (a), photoionisation (b), fluorescent emission of characteristic radiation (c), and non-radiative Auger process (d). Taken from [4].

Shown in Fig. 5 are the basic interaction processes of photons with matter: ionisation induced by electron collision, producing a scattered primary electron and a secondary electron in the process (a).

Photoionisation (b) was first described by Albert Einstein and refers to the emission of a bound electron by absorption of a photon of sufficient energy. The energy delivered by the incident photon has to exceed the binding energy of the electron, so that the leftover energy of the electron amounts to

$$E = \hbar\omega - E_B \tag{10}$$

Fluorescent emission of characteristic radiation (c) occurs after the excitation of a core electron,

leaving back a hole that is filled by an electron of a valence orbital by emission of energy

$$E_k - E_i = \hbar\omega \tag{11}$$

for a transition from the state i to the state k.

The non-radiative Auger process (d) is a second order process occurring if the emitted photon with energy $\hbar\omega$ is not released from the atom, but instead transfers its energy to another electron of the same shell as the one filling the core hole As such, fluoerescent emission and Auger emission are competing processes. The emitted photon in this process is called Auger electron.

2.2.2 Scattering, Diffraction, and refraction

Scattering

Diffraction

Bragg's law

$$m\lambda = 2d\sin\theta \tag{12}$$

Refraction is the turning of radiation at an interface of materials with different refractive index n

$$n = 1 - \delta + i\beta \tag{13}$$

For the X-ray regime, the (usually complex) refractive index deviates only slightly from unity. δ and β are typically of the order of $10 \cdot 10^{-5}$ or $10 \cdot 10^{-6}$.

Total external reflection is a phenomenon unique to the X-ray region of the spectrum. In this case, almost all of the incident energy is reflected at the surface, and it is possible to obtain it with a refractive index less then unity. Total external reflection occurs for angles θ at gracing incidence, following

$$\theta < \theta_c \approx \sqrt{2\delta} \tag{14}$$

2.3 Soft X-ray sources

While also portable X-ray tubes emitting photons in the soft X-ray region exist, the most common sources for soft X-rays are synchrotrons and X-ray Free Electron Lasers (XFELs). These are large research facilities usually requiring a cooperation of a multitude of universities, academia and companies with experts from a wide variety of fields.
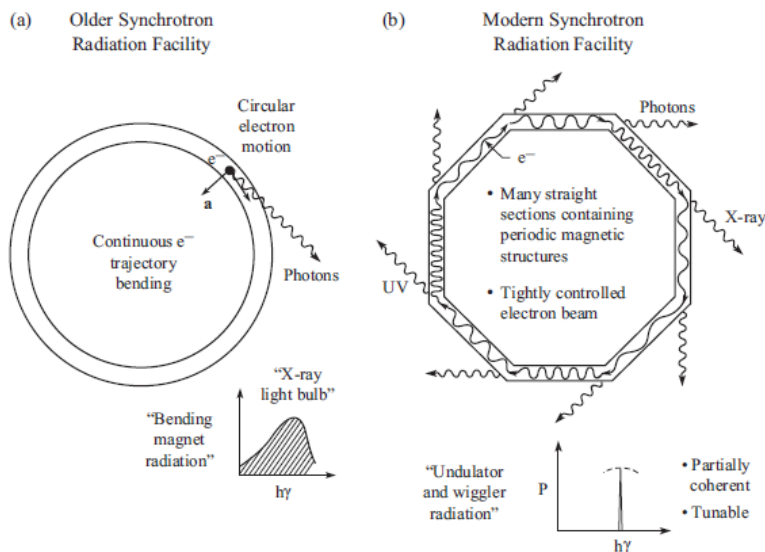
Figure 6: text

2.3.1 Synchrotron radiation

Fig. 6 depicts the outline of older and modern synchrotron radiation facilities. In both cases, electrons are forced on a circular trajectory by application of magnetic fields. Radiation is produced by means of constantly accelerating electrons at relativistic speed. As is shown in the figure, at the advent of synchrotron radiation, bending magnets were used to continuously force an electron on a circular orbit. In contrast, a modern synchrotron facility or storage ring consists of many straight sections containing periodic magnetic structures, called insertion devices (ID), which are connected by bending magnets.

Synchrotron radiation has many desirable properties, such as

- high photon flux

- high brilliance

- high stability

- polarisation control

Furthermore, users at synchrotron facilities are able to select the wavelength necessary for their applications and experiments from a broad spectrum, ranging from microwaves to hard X-rays.

15

(a)

$\theta = \frac{1}{2\gamma}$

A

B

$R\sin\theta$

$\theta = \frac{1}{2\gamma}$

Radius R

$\theta = \frac{1}{2\gamma}$

The cone half angle
θ sets the limits of
arc-length from which
radiation can be
observed.

(b)

B′

I

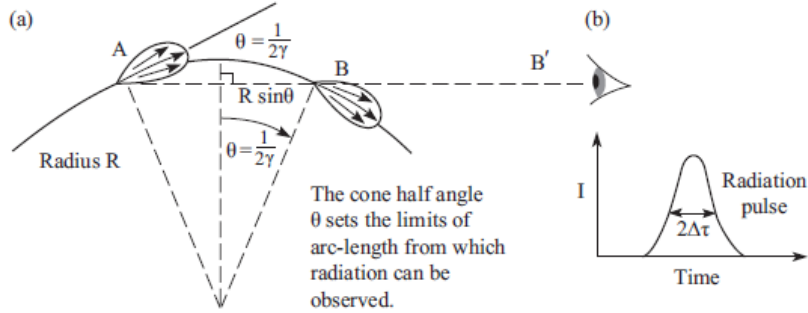Radiation
pulse

$2\Delta\tau$

Time

Figure 7: text

Synchrotron radiation is a special case of bremsstrahlung and refers to continuous radiation emitted from relativistic electrons moving on a circular orbit. The electrons can be forced on a circular orbit using magnets, if the contributions from both the Lorentz force and the centripetal force are equal:

$$evB = \frac{mv^2}{R},$$ (15)

with e, v, and m being the eletron charge, electron speed, and relativistic electron mass, respectively, B the magnetic field, and R the circumference of the circular orbit.

Fig. 7 illustrates the radiation resulting from such an electron motion. At relativistic speed, radiation is emitted by the electron in a narrow cone in forward direction of half angle

$$\theta = \frac{1}{2\gamma}$$ (16)

$$\gamma = \frac{1}{\left(1 - \frac{v^2}{c^2}\right)^{\frac{1}{2}}},$$ (17)

hence giving it the name "searchlight" radiation. The first synchrotron radiation facilities employed this basic principle to deliver radiation comparatively high in flux and brilliance and low in emittance.

However, compared to these facilities, modern storage rings now use more sophisticated technology, further improving on the advantages of synchrotron radiation. As shown in Fig. 6, they consist of many straight sections connected with bending magnets. These so-called insertion devices are long periodic magnetic structures that can be inserted into and removed from the ring quite easily. They can be divided into two types: wigglers and undulators.

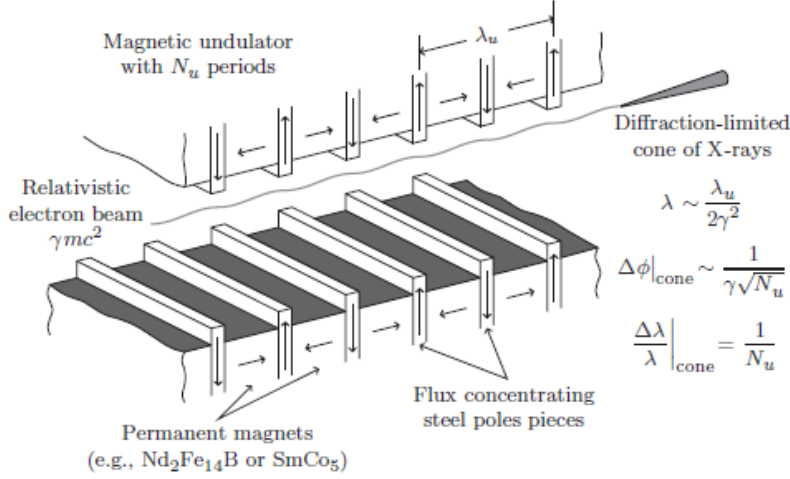Fig. 8 gives an impression of an undulator ID. It consists of a periodic structure of dipole

16

Figure 8: Taken from [5].

magnets such that the magnetic field along the undulator is alternating with the wavelength λ_u. By applying this alternating magnetic field, an electron traversing the undulator has to undergo periodic oscillations, thus radiating energy at every turn. The radiation produced by an undulator is very narrow and of high intensity compared even to bending magnet radiation.

The wavelength of the undulator radiation is given by the undulator equation,

$$\lambda = \frac{\lambda_u}{2\gamma^2}\left(1 + \frac{K^2}{2} + \gamma^2\theta^2\right) \tag{18}$$

where the motion of an electron in the ID is described by the undulator strength parameter,

$$K = \frac{eB\lambda_u}{2\pi m_e c}, \tag{19}$$

with m_e the electron rest mass and c the speed of light. For $K << 1$ we speak of an undulator, where the oscillation amplitude of the electron is small, leading to interference patterns in the radiation spectrum and thus to narrow energy bands. An exit slit is then filtering the all the cones except for the central one. For $K >> 1$, the ID is called a wiggler. In this case, the oscillation amplitude is larger, leading to a broad spectrum.

Undulators deliver several orders of magnitude higher flux than simple bending magnets. For an undulator with N periods, the brightness of the beam can scale with up to N^2. Due to the narrow energy band produced by an undulator, the spectrum usually becomes monochromatic.
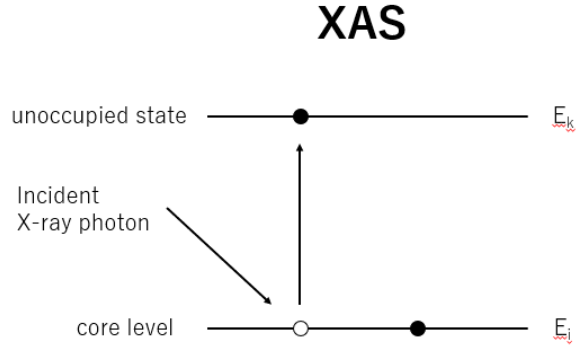
XAS

Figure 9: text

2.3.2   The X-ray Free Electron Laser

Free electron lasers (FELs) are employing the undulator technology, further improving the bright-
ness and brilliance of the beam and narrowing the emitted radiation though finer control of the
relativistic electron bunches traversing the undulator. Although employing a mechanism completely
different from typical lasers, they derive their name from similar physical properties achieved with
electrons moving freely in the periodic magnetic structure, hence FEL. They also obey the undu-
lator equation (Eq. 18). The central radiation cone,

$$\theta_{cen} = \frac{1}{\gamma\sqrt{N}}, \tag{20}$$

includes a $1/N$ spectral bandwith centered on λ, where N is the number of undulator periods.
Attributing to the higher number of undulator periods compared to an undulator in a synchrotron,
FEL radiation possesses higher peak power, shorter pulses, has a highly coherent spectrum and a
much smaller radiation angle.

In principle, FELs can operate across a wide range of the electromagnetical spectrum, from
infrared light to hard X-rays. FELs operating in the X-ray regime are called XFELs.

2.4   Soft X-ray Spectroscopy

2.4.1   X-ray Absorption Spectroscopy (XAS)

During X-ray Absorption Spectroscopy, the geometric and electronic structure of matter is probed
with an energy-tunable incident photon beam. The incident photon is absorbed by a deep core
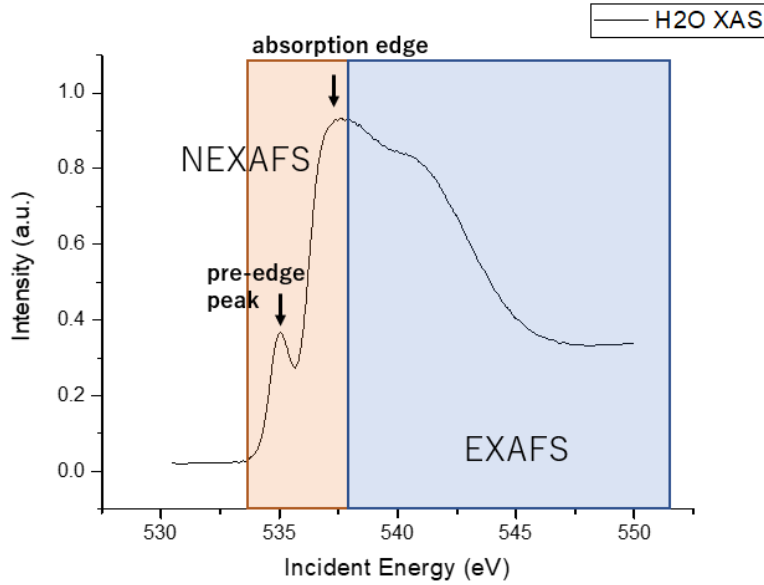
Figure 10: XAS O K-edge spectrum for liquid H_2O, with NEXAFS and EXAFS regions marked orange and blue, respectively. Taken and modified from [6].

level electron (Fig. 9), which is excited to an unoccupied state according to the equation

$$E_i - E_k = \hbar\omega, \tag{21}$$

where ω is the frequency of the incident photon with the energy

$$E = \hbar\omega, \tag{22}$$

and i and k, $i \neq k$ are the respective atomic energy levels. XAS is element-specific, depending on the incident energy chosen. The spectrum is recorded measuring the absorption coefficient of the sample and provides information about the unoccupied states of the sample material. The absorption coefficient of a material,

$$\mu = \ln\frac{I_0}{I_T}, \tag{23}$$

with I_0 the initial and I_T the transmitted intensity, is measured during an XAS experiment in transmission mode. Another possibility to get the absorption is to measure the total fluorescence yield of the sample.

Fig. 10 shows a typical absorption spectrum. It can be divided into two distinct parts providing

19

XES

occupied state ●————● E_k

Characteristic emission
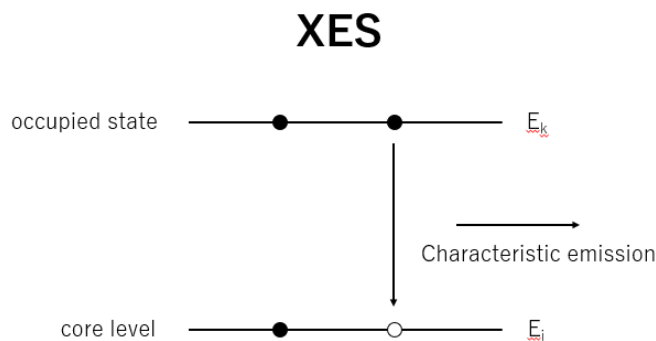
core level ●————○ E_i

Figure 11: text

different information about the sample geometric and electronic structure.

Near-Edge X-ray Absorption Fine Structure (NEXAFS) refers to the absorption edge and the region right before the abrupt rise in the absorption coefficient. The absorption edge itself gives information about the 1s ← np continuum state transitions, while the pre-edge peak a few eV below the absorption edge hints towards non- or anti-bonding states. In the case of bulk liquid water, as in Fig. 10), it scales with the amount of broken hydrogen bonds in the liquid.

Extended X-ray Absorption Fine Structure (EXAFS) starts at energies right above the absorption edge. Here, the photoelectron is excited significantly above the binding energy of the atom, thus leaving the excited atom and scattering off the neighbouring atoms. The original and the scattered wavefunction then undergo interference, visible in the spectrum. EXAFS gives information about the long-range interactions in the sample.

2.4.2   X-ray emission spectroscopy (XES)

X-ray emission spectroscopy (XES) is the follow-up process after a core-level electron was excited (by absorption of a photon, for example) and as such is a complementary technique to XAS. The core hole created through this process is filled immediately (τ ~fs) by an electron of a valence shell and the difference in energy is released by fluorescence emission of a photon. A spectrum is recorded by detecting the photons emitted from the sample, which gives information about the occupied electronic states of the material under investigation. Usually, XES is a non-resonant technique, that is, the incident energy does not have to be tuned as long as it is above the absorption edge.

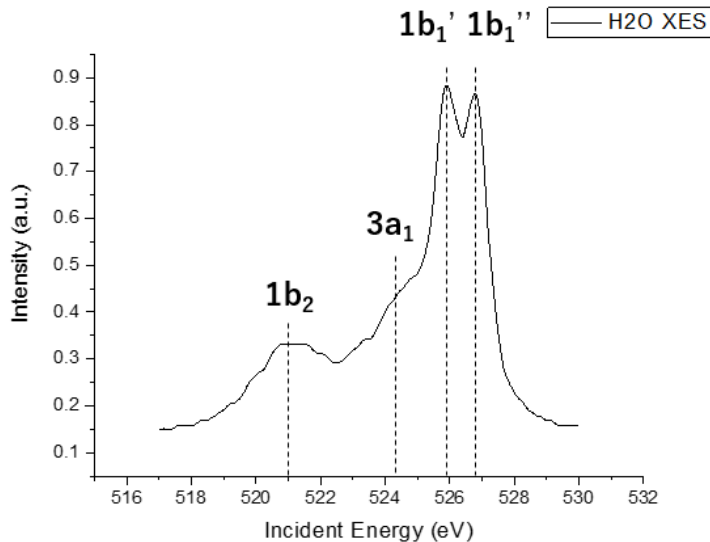The XES spectrum of bullk liquid water is shown in Fig. 12, exhibiting four distinct peaks

Figure 12: XES O K-edge spectrum of liquid H_2O.

clearly separated from each other. These peaks correspond to transitions from the $1b_2$, $3a_1$, and $1b_1$ molecular orbitals of H_2O to the ground state. The splitting in the peak indicates the presence of different structural species in the bulk liquid [7][8]. Generally speaking, XES is very sensitive to the chemical environment of the excited atom and is thus of particular use to investigate these changes, which are imprinted into the spectral structure of the emitted fluorescence.

2.4.3 Resonant Inelastic X-ray Scattering (RIXS)

Resonant Inelastic X-ray Scattering (RIXS) is a two-step process (Fig. 13) and the combination of the two above mentioned processes, XAS and XES, on resonance. This means that the incident energy is tuned in the vicinity of an absorption edge, which is followed by changes in the emission spectrum depending on the excitation energy.

Starting from the initial state, an incident photon of energy $\hbar\nu = \Omega$ and momentum $\vec{k}$ is absorbed by a core level electron, which is excited to the valence band. This leads to the creation of a short-lived intermediate state with a core hole. As in XES, the core hole is subsequently filled by an electron from a valence state via emission of a photon of energy $\hbar\nu = \omega$ and momentum $\vec{k'}$, thus the atom is relaxing to the final state. During RIXS, the energy and the momentum transfer
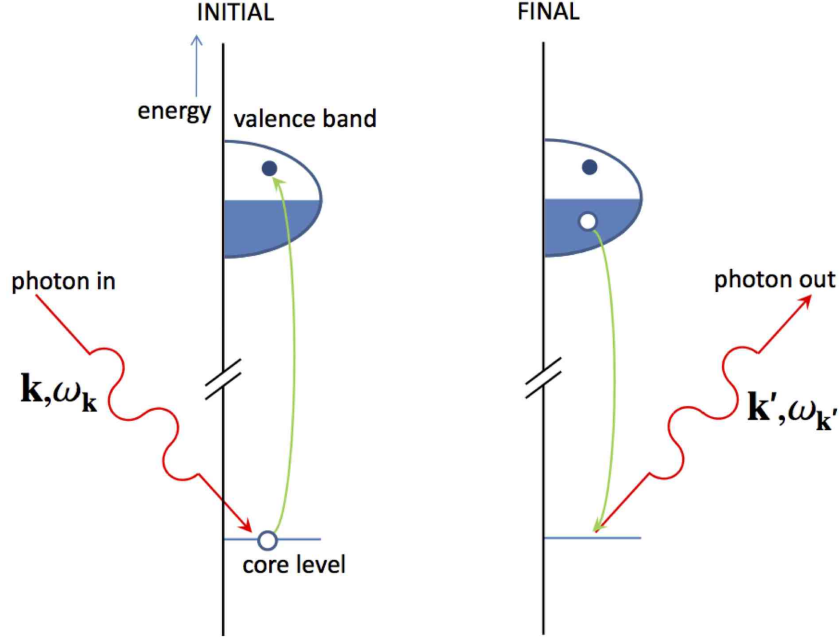
Figure 13: Basic emission and absorption processes of photons interacting with matter.

between incident and emitted photons,

$$E_T = \Omega - \omega, \tag{24}$$

$$Q = \vec{k} - \vec{k'}, \tag{25}$$

are recorded and used to create a two-dimensional map.

Fig. 14 shows a typical RIXS map of bulk liquid water at the oxygen K-edge. The intensity is plotted in 2D over the excitation and emission energy. It also shows the fine structure of the $1b_1$ peak, also visible in the XES spectrum (Fig. 12), at $540\,\text{eV}$. However, thanks to increased sensitivity and enhanced resolution, it is also able to detect a different shape of the peak right above the onset of absorption.

RIXS is a very powerful technique for measuring small changes and excitations of the electronic structure of the order of a few eV or less. As such, RIXS enjoys high popularity especially in the field of condensed matter physics, being capable of measuring charge transfer excitations and d-d transitions as well as elementary excitations of magnons and phonons of transition metal oxides. Since the energy scale involved here is very small and requires a high resolving power of the instrument, RIXS spectrometers currently under construction strive to achieve ever higher
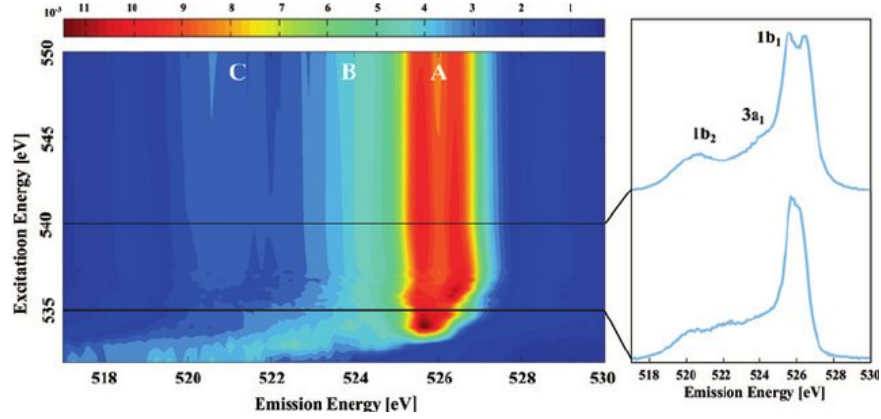
Figure 14: Taken from [9].

resolution, with the top at $\Delta E/E = 100\,000$ [10].

2.5 Soft X-ray optics

2.5.1 Mirrors

2.5.2 Monochromators

2.5.3 Reflection Gratings

Reflections gratings have both reflective and diffractive effects on photon beams hitting their surface. They are key parts in beamline and spectrometer applications, enabling the energy-dispersive or wavelength-dispersive selection of X-ray photons and thus the simultaneous detection of photons with distinct energy. Typically reflective gratings are manufactured using mechanical ruling methods, which cut a series of grooves at specified angles. They obey the grating equation,

$$\sin\alpha - \sin\beta = a_0 k\lambda, \tag{26}$$

with α and β the angles of incoming and outgoing beam with wavelength λ (measured from the surface normal), a_0 being the constant ruling density on the grating surface, and k the diffraction order of the reflected beam ($k = 0, \pm 1, \pm 2, \pm 3$). The incoming beam with wavelength λ is dispersed according to this equation.

The geometry of the reflection grating is illustrated in Fig. **??**. Typically, improved performance in comparison to a grating with constant groove density is achieved with a varied-line space (VLS) grating. The grooves of a VLS grating are ruled on the surface with a local groove density n, following the equation
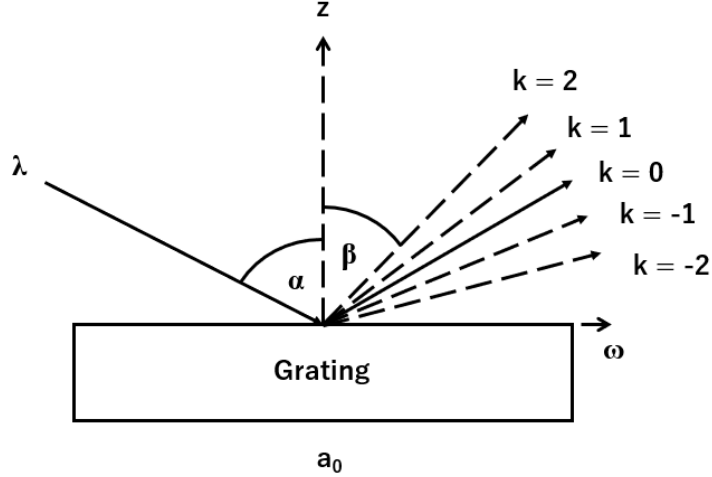
23

Figure 15: Sketch of a reflective grating with the most important parameters. α and β are the angles of the incoming and outgoing beam with wavelength λ, respectively, a_0 is the constant ruling density of the grating, and k is the diffraction order ($k = 0, \pm 1, \pm 2, \pm 3$).

$$n(\omega) = a_0 + a_1\omega + a_2\omega^2 + a_3\omega^3 + ..., \tag{27}$$

where ω refers to the coordinate in direction of beam propagation and a_0, a_1, a_2, a_3,... are the coefficients of the local groove density expansion.

2.6 SPring-8 Beamline BL07LSU for soft X-ray spectroscopy

The University of Tokyo Synchrotron Radiation Research Center currently is operating the soft X-ray beamline BL07LSU at SPring-8 (short for Super Photon Ring - 8 GeV), located in Harima in Western Japan [11]. One of the research focii is the investigation of water and its unusual properties, as well as the investigation of spintronics of transition materials. To that extent, the beamline is equipped with three different endstations, enabling its users to perform XPS, ARPES, RIXS, XAS and XES experiments, among others, plus a free-port station, allowing users to bring their own equipment and spectrometers.

One of these endstations is the high-resolution spectrometer HORNET, which was built to achieve an energy resolution of about 10 000 at the reference energy of 600 eV [13].
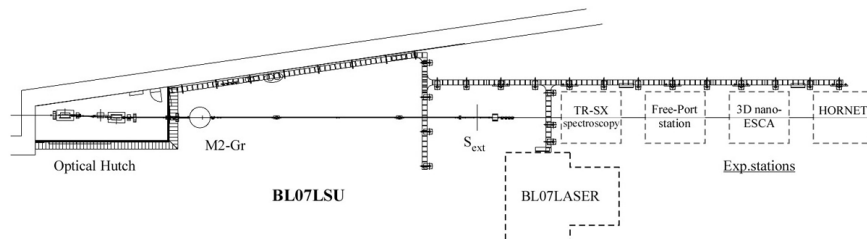
Figure 16: Sketch of BL07LSU and its endstations. Taken from [12].

2.7 Theoretical foundations of XES spectrum calculations

2.7.1 Molecular Dynamics simulations

A Molecular Dynamics (MD) simulation is the simulation of the simultaneous motion of a set of atomic nuclei and their respective electrons. Without any approximations, this in principle would require the solution to the full time-dependent Schroedinger equation for both the electronic und nuclear degrees of freedom.

In practice, even with today's computational power, this is unfeasible for systems of more than three atoms. Therefore, we need to simplify the approach by introducing appropriate approximations. First of all, we make the assumption that it is possible to separate the motions of the nuclei and the electrons, and that the electron motion adapts instantaneously to any change in the nuclear configuration. As a consequence, the nuclear motion evolves on a potential energy surface (PES) that is associated with the electronic quantum state obtained by solving the time-independent Schroedinger equation for the electrons for a series of nuclear geometries. This approximation is known as the Born-Oppenheimer approximation, hence we speak of Born-Oppenheimer molecular dynamics. Most MD simulations are performed on the ground-state PES.

Furthermore, atomic nuclei in MD simulations are treated as classical particles with trajectories calculated using the laws of classical mechanics. The interatomic potentials are found as the solutions to the electronic structure problem in each MD step for a particular configuration of the atomic nuclei. This amounts to solving the time-independent Schroedinger equation for the electrons, while the nuclei propagate along classical MD trajectories. The equations of motion

$$M_i \ddot{q}_i = -\boldsymbol{\nabla}_i min_\Psi \langle \Psi | H | \Psi \rangle , \tag{28}$$

where $H\Psi = E\Psi$ is the time-independent Schroedinger equation for the electrons, H the Hamiltonion, and M_i and $\ddot{q}_i$ the mass and the acceleration vector of the ith nucleus. In each step, the minimum of $\langle H \rangle$ has to be reached by calculating the electronic wavefunction by means of density functional theory [14].

25

2.7.2 Semi-classical Kramers-Heisenberg formalism

To correctly calculate the emission spectra of a target molecule, the core-hole-induced dynamics have to be taken into account. The Kramers-Heisenberg (KH) formula for a non-resonant transition,

$$\sigma(\omega') = \sum_j \left| \sum_n \frac{\langle f| D' |n\rangle \langle n| D |i\rangle}{\omega' - E_{nf} + i\Gamma} \right|^2,$$ (29)

includes vibrational broadening and interference effects that are anticipated by the excitation of a core electron to an excited state. i, n and f refer to the initial, the intermediate, and the final state, respectively. D and D' are the corresponding transition dipole operators for the transitons $i \to n$ and $n \to f$, with Γ the line broadenig parameter.

However, Eq. 29 requires the calculation a full set of vibrational eigenstates for each electronic state. While this can be done for a system with only a few degrees of freedom, calculational expenditure scales with the number of degrees of freedom. Therefore, approximations reducing the computational cost are desired.

As shown in [15], using a semiclassical approximation to the KH formula (SCKH) is in good agreement with the results for the full quantum wavepacket dynamics calculation. Within the semi-classical approximation, time evolution is being treated classically as a sum of classical trajectories on the intermediate potential energy surface (PES), but started from a sampling of ground-state quantum distributions of position and momentum.

The approximated expressions of the KH formula used in the spectrum calculations are

$$\sigma^{class}(\omega') = \sum_{traj} \sum_F \left| D_F^{+class}(\omega') \right|^2$$ (30)

and

$$D_F^{+class}(\omega') = \int_0^{\inf} dt D_{NI}^+(0) D_{FN}'^+(t) \exp^{-i \int_0^t (E_F(\tau) - E_N(\tau)) d\tau} e^{-\Gamma t} e^{-i\omega' t}$$ (31)

Eq. 30 takes into account vibrational effects from the intermediate and final states and thus includes interference of the intermediate-state wave functions in one step.

26

3 Analysis of Lithium Hydrate Melt

3.1 A room temperature hydrate melt

Already mentioned in the previous chapter, a "water-in-salt" or hydrate melt aqueous electrolyte is a metal salt that forms a liquid by addition of only a small amount of water, in which all the H_2O molecules are coordinated with the metal cations [16]. Therefore, interactions between ions become much more prominent in comparison to ion-solvent interactions, leading to unusual physiochemical properties. Such salt-water mixtures with Li^+ cations are usually only fluid far above room temperature ($>100\,°C$), thus rendering them useless as an application for aqueous lithium-ion batteries.
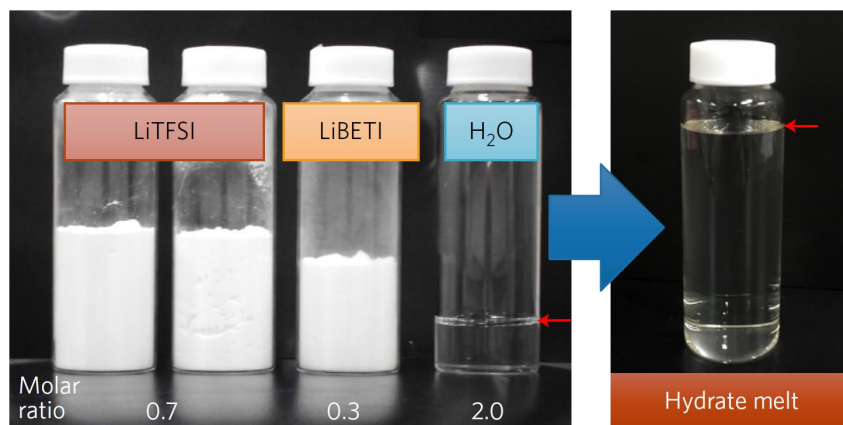
Figure 17: Picture showing the molar mixing ratio of .

However, by addition of a well defined amount of imide anions, in this case, bis(trifluoromethane)sulfonimide ($N(SO_2CF_3)_2^-$, TFSI) and bis(pentafluoroethylsulfonyl)imide ($N(SO_2CF_5)_2^-$, BETI), a hydrate melt at room temperature becomes available.

Of great interest is the exact structure of the molecules and the coordination of the oxygen atoms to the Li^+ cations in the hydrate melt. Sharp peaks in Raman spectroscopy of this Li hydrate melt indicate that water molecules are hydrated to the Li^+ cations rather than forming water clusters in the liquid [3], thus possessing a main donating-/accepting-like stretch in the spectrum. The same Raman spectra indicate that the coordination number of Lithium is four, that is, every Li atom in the liquid is surrounded by four molecules. However, how exactly H_2O bonds with other radicals so as to form a liquid and how Li behaves in the hydrate melt are open questions. To shed light on this, XAS and XES in the soft X-ray range were considered appropriate tools to probe the underlying structure of the liquid. XES is sensitive to the donating hydrogen bond, while XAS is
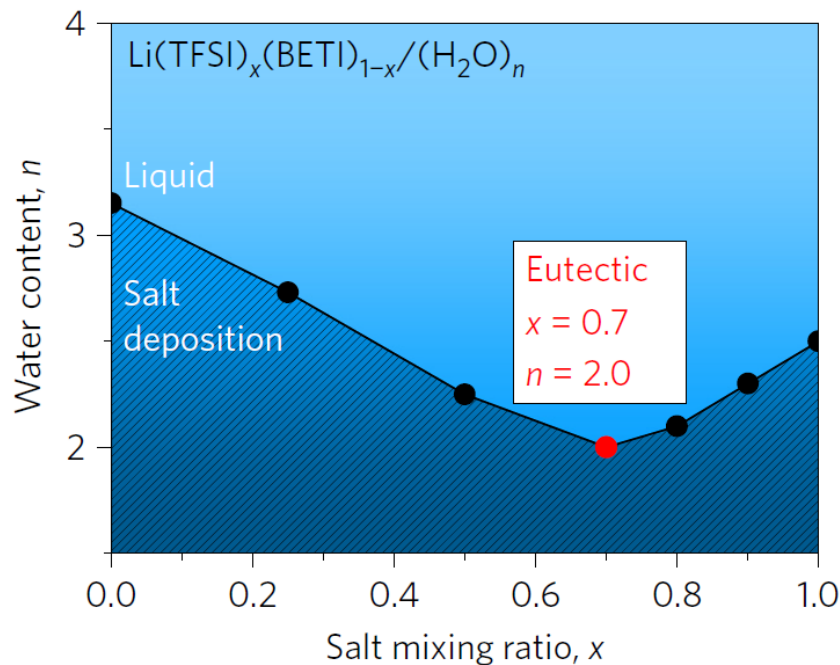
Figure 18: Mixing ratio of H_2O, Li^+, TFSI and BETI necessary to obtain room temperature hydrate melt.

sensitive to the accepting hydrogen bond. Comparing the hydrate melt spectrum to those of the metal salt powder and liquid H_2O should provide essential clues as to which structure is emerging in the hydrate melt and why it possesses this level of electrical conductivity. To provide support from the theoretical side, these experiments are accompanied by theoretical calculations of X-ray emission spectra.

3.2 Experiment

O K-Edge XAS and XES spectra of several hydrate melt-related samples have been measured, with the goal of better understanding the interactions between water, Lithium and the anions the hydrate melt consists of. The experiments were carried out at SPring-8 soft X-ray beamline BL07LSU and the RIXS spectrometer HORNET.

3.2.1 Experimental Setup

3.2.2 Sample preparation

The experiment was carried out using the following samples: purified liquid H_2O, Li−TFSI and Li−BETI powder, liquid mono hydrate melt made of x mol H_2O and y mol LiTFSI, and liquid
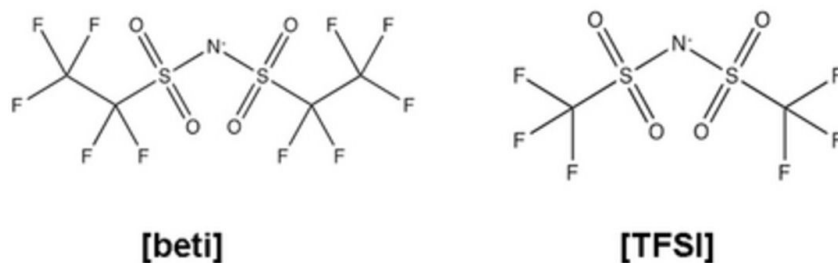
Figure 19: The two organic imide anions, $N(SO_2CF_3)_2^-$ (TFSI) and $N(SO_2CF_5)_2^-$ (BETI), used in the room temperature Li hydrate melt.

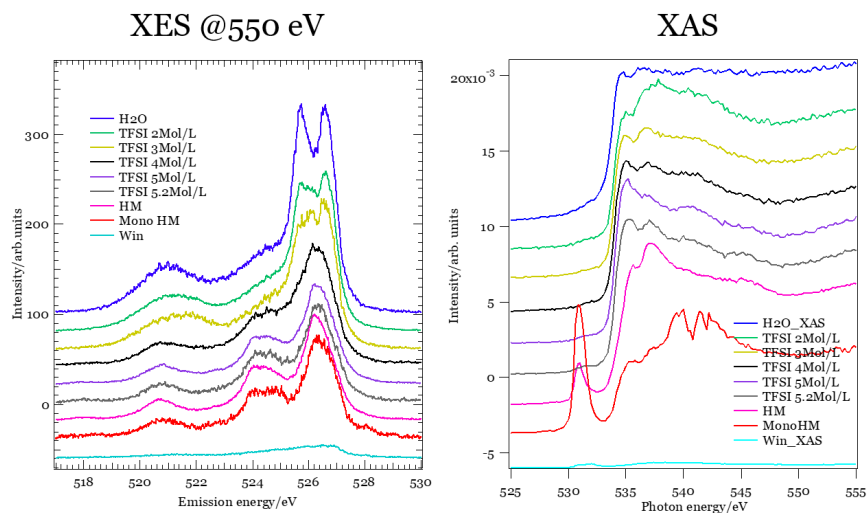
Figure 20: text

hydrate melt with the chemical formula $2\,H_2O-Li(TFSI)_{0.7}(BETI)_{0.3}$.

While preparing the both the hydrate melt samples, great care had to be taken to prevent oxygen contamination of the hydrate melt. To that extent, these samples were prepared with great care in a clean and oxygen-free environment and inserted into the liquid cell.

3.2.3 Results

3.3 Theoretical Calculations of X-ray emission spectra

To support the evidence of the assumed acceptor- and donor-like structure of Li and H_2O in the liquid hydrate melt, theoretical calculations of XES spectra were carried out. Such calculations have already been successfully performed on H_2O and other liquid structures and have been ca-
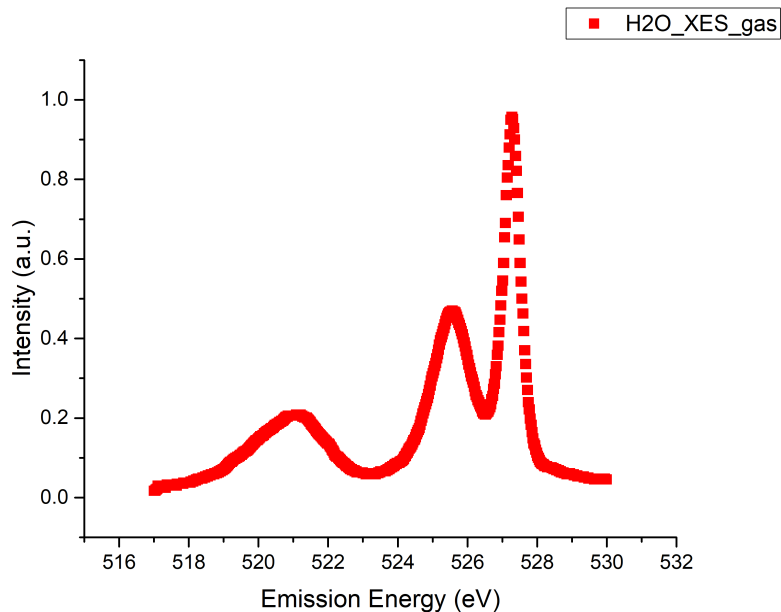
Figure 21: text

pable of reproducing the experimentally obtained XES spectra with excellent agreement [17]. A similar theoretical calculus was developed as described in this reference, and used to calculate the XES spectra of small clusters including Li^+ and H_2O obtained from ab initio molecular dynamics simulations. First, the method is described in detail, after which the results are being presented.

3.3.1 Structural analysis

For a basic analysis of the structure of the $Li(TFSI)_{0.7}(BETI)_{0.3}$ hydrate melt, it is instructive to follow a few simple considerations before trying to calculate the spectra from the whole cluster.

By subtracting the contribution of TFSI and BETI to the total spectrum, it was thought that the contribution of the remaining Li and H_2O can be evaluated. Comparing the resultant spectrum to that of liquid water, one can observe some features apart from different peak intensities that distinguish the $Li-H_2O$ spectrum from the pure liquid water spectrum. First, with the addition of Li^+, the second peak shifts slightly towards lower energies

Sample structures containing 40 H_2O molecules, 20 Li^+ cations, 14 TFSI and 6 BETI were modeled after the obtained room temperature Li hydrate melt mixture 18, and the molecular dynamics (MD) of this system was simulated. The total atom count of the system is 769. In total, four 2 ps long MD simulations were performed, with a time interval of 0.25 fs. This procedure
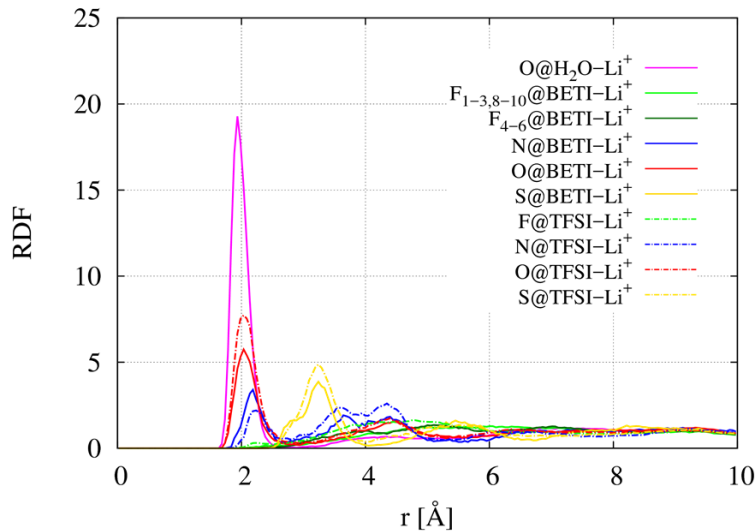
Figure 22: The radial distribution function (RDF) of every atom type present in the hydrate melt structure as a function of distance to the Li^+ cation.

yielded altogether $80\,000$ snapshots of the hydrate melt structure. To process such a huge amount of data is a rather heavy burden, and thus, cluster analysis and principal component analysis was used to extract meaningful information from this data.

Furthermore, the radial distribution function (RDF) of the different types of atoms present in the structure as a function of the distance between the atom and the closest Li^+ cation has been obtained (see Fig.) 22). From the RDFs one can deduce that the favoured bond of Li^+ is to the oxygen atom of an H_2O molecule, with the most probable bonding distance centered at around $2\,\text{Å}$. This fosters the assumption that the largest contribution the emission spectrum of Li hydrate melt comes from Li^+ coordinated to water molecules.

Further analysis focused on each H_2O molecule in the structure and their respective surroundings. Structures were obtained centering on these water molecules and including all other atoms and molecules within a sphere of a $3\,\text{Å}$ cutoff radius. Thus, several structures of different sizes were obtained and classified according to the number of Li atoms they are including. These structures served as a basis for XES calculations.

3.3.2 Methodology

Using the above described classified structures as a basis, the spectra were calculated using the deMon2k code, which is capable of performing MD simulations as well as calculating the transition dipole moments needed for the calculation of XES and XAS spectra [18]. For calculating the spectra
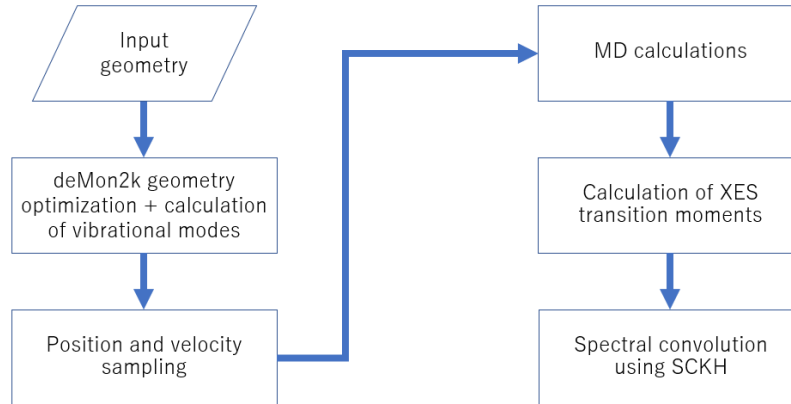
Figure 23: text

from the transition moments, the SCKH code by Mathias Ljungberg was used [**?**].

For an overview of the calculational scheme, refer to Fig. 23. Sample structures were taken using the above described procedure and for each structure, the O atom of the respective H_2O molecule at the origin was targeted for core-hole excitation. In each case, geometry optimisation was performed on the target molecule, followed by a partial vibrational analysis with all atoms except for the target H_2O fixed. This ensured that the three highest vibrational modes correspond to the vibrational modes of the target water molecule. Then the quantum initial distribution of position and momenta of every atom in the structure was sampled for each of the vibrational modes. It turned out that the sampling of a set of three initial positions and four initial velocities suffices to average out sharp features of the spectrum depending on only one position or velocity sampling. The Born-Oppenheimer molecular dynamics of these systems were recorded on trajectories 40 fs long with a time interval of 0.25 fs, resulting in 160 time points in total. Along these trajectories, core-hole excitation was performed and subsequently transition moments were calculated. Using the above mentioned SCKH code, spectra were calculated assuming a core-hole life time of 3.6 fs [19], corresponding to a spectral broadening of 0.18 eV.

All the calculations were run on a workstation at Heian university with the help of Dr. Ying Guoling. Using this computational power, it was possible to calculate the emission spectra in a reasonable amount of time.

3.4 Results

3.4.1 $Li^+ - H_2O$

3.4.2 $Li^+ - 2\,H_2O$

3.5 Hydrate melt constituents

3.5.1 Structures without Li

Without exception, the 60 structures without Lithium consisted of one H_2O molecule and one TFSI molecule. TFSI has a rather strong impact on the shape of the spectrum. Analysis of the several spectra, albeit proving difficult to the multitude of possible configurations, yielded that the relative peak intensities are dependent on the closest neighbouring atom to the oxygen atom of the H_2O molecule. If the closest neighboring atom to the H_2O oxygen is F, the intensity of the third peak is usually larger than the intensity of the second peak. In case of the closest neighbouring TFSI atom being O, it is the other way round.
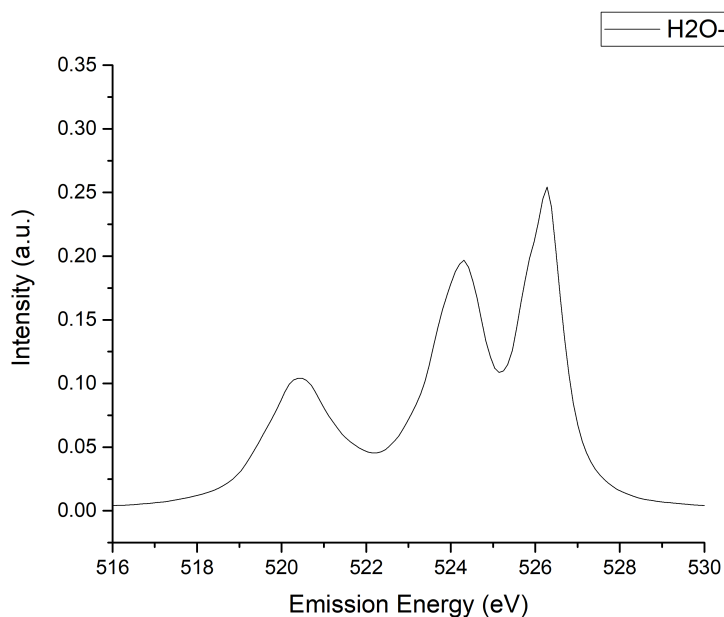

Figure 24: text

Fig. 24 shows the spectrum averaged over all H_2O-TFSI structures.

3.5.2 Structures with one Li$^+$ cation

The structures containing one Li$^+$ cation can be devided into two main classes: Lithium with n H$_2$O molecules coordianted to it ($n = 2, 3, 4$), and Lithium together with one H$_2$O and one TFSI molecule. Analysis of the spectra and their respective geometrical structures structures in this case proves difficult due to their complexity.
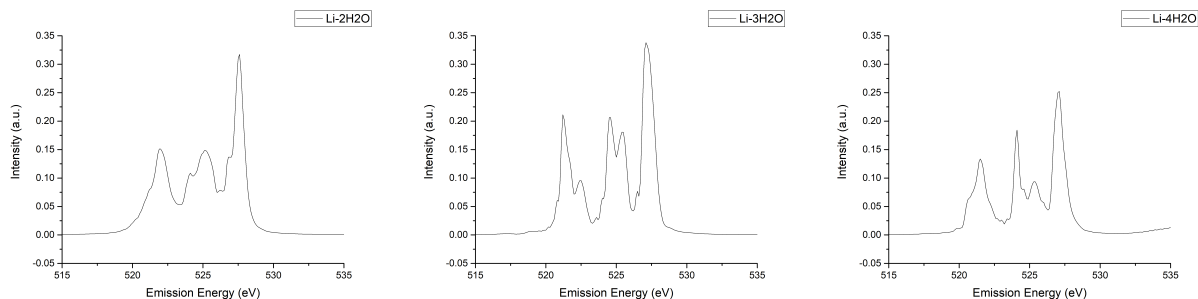
- Li−nH$_2$O

Figure 25: text

The number of structures 18, 2 and 3 for n equaling 2, 3 and 4 respectively. Compared to pure water, the spectrum gets heavily distorted depending on the distances between the H$_2$O oxygen and the Li$^+$ cation as well as the O of the other water molecules (Fig. 25). The change does not change much with respect to the number of water molecules contained in the cluster.

- Li−H$_2$O−TFSI

As seen in Fig. 26, the addition of TFSI to the cluster heavily affects the spectrum, smearing out the formerly distinct peaks. Here, there also seems to be a connection between the distance of Li and O of the water molecule and the intensity of the third peak - the larger the distance, the more intense the peak.

3.5.3 Other structures

Clusters with two Li atoms were excluded from the analysis, since the calculation of the RDF did not show any traces of Li bonding to each other.

3.5.4 Combination of spectra

The next logical step towards the reproduction of the experimental spectra was the combination of the obtained theoretical spectra following careful considerations of the various contributions of
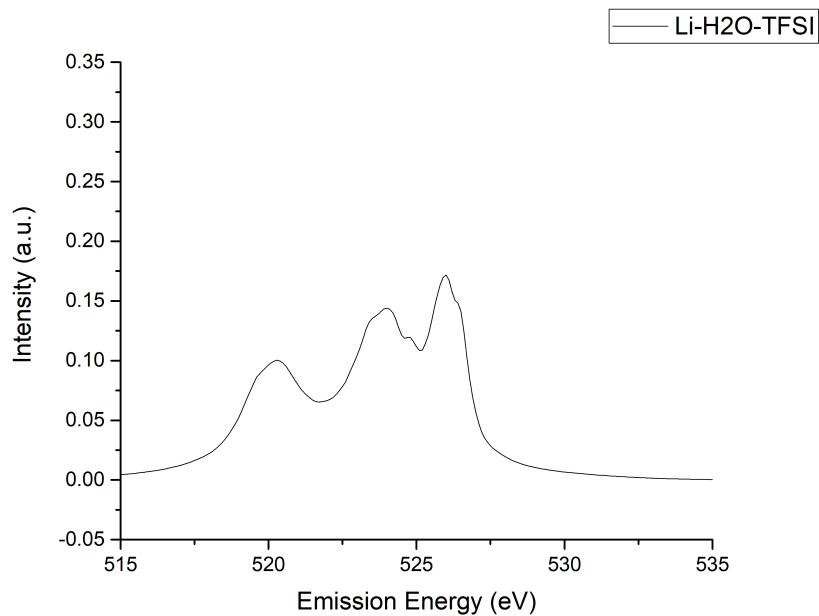
Figure 26: text

the different structures.

Fig. **??** shows an attempt of the calculation of the contribution of the water molecules in the hydrate melt mixture. Even though simplified structures were used for the calculation of theoretical XES spectra and given the complexity of the analysis, the combined result of the different structures is able to reproduce features already seen in the experiment, such as the shift of the second peak towards lower energies and the small shoulder at the lower end of the second peak. However, other features, like the small contribution at 518 eV, do not appear in this analysis. For a more accurate description, more complex structures and the contribution from the TFSI and BETI O atoms have to be taken into account.

4 Numerical optimisation of spectrometer geometry and VLS grating

4.1 SLiT-J (Synchrotron Light in Tohoku - Japan)

SLiT-J [20] is the name of a future 3 GeV synchrotron facility in the Tohoku region in the east of Japan, which is scheduled for construction starting from 2019. Its design concept envisions a synchrotron light source with low emittance (0.93 nm) and a brilliance in the soft X-ray region that is a 100 times higher than that of SPring-8, while its operation will only consume about one tenth of the power that is needed for the operation of SPring-8. The University of Tokyo Synchrotron Radiation Center, which is currently responsible for the operation of the BL07LSU beamline at SPring-8 [11], will take part in the construction and operation of a new beamline at the future synchrotron. Since the research focus at BL07LSU is on soft X-ray spectroscopy, it makes sense to migrate from SPring-8 to the new synchrotron. Not only will the new synchrotron feature improved beam parameters, but also due to the shift from 8 to 3 GeV more radiated photons will be in the wavelength corresponding to soft X-rays, greatly increasing the efficiency of the beamline. As a part of this project, it is planned to install two XES spectrometers: one with high efficiency and another one with ultra-high resolution, meeting or even exceeding $\frac{E}{\Delta E} = 100\,000$.

While the spectrometer with high efficiency will essentially be an upgraded version of the spectrometer called HORNET, currently in operation at SPring-8 beamline BL07LSU, which will be moved to the new synchrotron facility once it commences operation, the high-resolution spectrometer will be based on an entirely new concept and constructed from scratch. However, in both cases, for conceptual planning, it is necessary to measure the effect of the upgraded or newly used spectrometer optics and to define the underlying parameters of the spectrometer geometry before actually constructing it. Ray-tracing codes have proven themselves a useful and reliable tool aiding this conceptual phase.

The goal was to calculate reasonable beamline optics for the two mentioned XES spectrometers. At first, we start with a small introduction to the ray-tracing code SHADOW, then discuss the XES spectrometer geometry and the road to optimising this geometry and the corresponding optical parameters. At last, the results of the calculations are presented.

4.2 Ray-tracing

It should be emphasised again that, prior to the construction of any X-ray instrument, as, for example, a new beamline at a synchrotron radiation source, any designer in charge has to think about the conceptual design of the optics he wants to use. The beam of the source is to be propagated using different kind of optics to an image plane, typically the position of the target.

Any calculation of this beam propagation has to incorporate the physical properties of the beam, such as its divergence and angular distribution, as well as the properties of the optics, such as surface errors of mirrors and ruling errors of gratings, to show the beamline designer which parameters are feasible to use in order to fulfil a certain scientific requirement, such as high intensity, high energy resolution, or a compromise between those two.

A feasible and very useful tool in this respect are ray-tracing codes that are capable of modeling different kinds of light sources and optical elements and trace the beam position on each of these elements or any arbitrary image plane in real space as well as in phase space. These days, those codes include several tools to model ever more sophisticated optics and allow the user to write his own macros or even to use his own code.

In this thesis, the program XOP and its extension SHADOWVUI were used for ray-tracing of all X-ray optical systems. The underlying ray-tracing engine for these codes is SHADOW in its 3rd revision, based on a geometrical ray-tracing approach [21][22][23]. SHADOW3 is publicly available [24] and widely used in the community of synchrotron radiation and X-ray optics. It is easy to use and has proven successful in the design of dozens of beamlines and spectrometers using a wide variety of optical elements around the world.
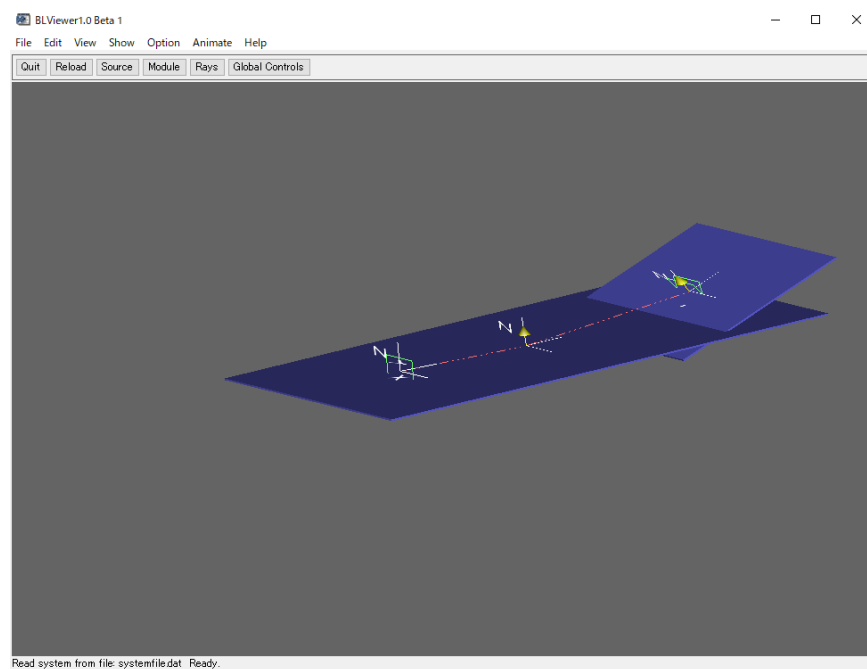

Figure 27: The optical elements of a model spectrometer, as displayed in ShadowVUI. From left to right: source, grating, and detector.

Using shadow, it is quite simple to define optical elements, render them (Fig. 27) and to show
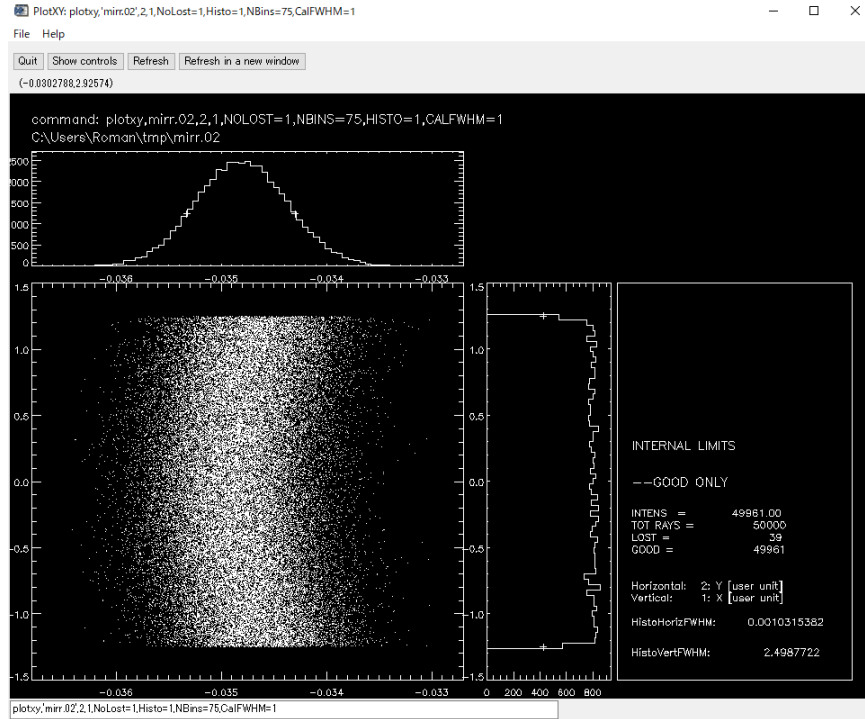
Figure 28: A typical footprint on the detector calculated by the SHADOW3 ray-tracing code.

the position of the traced rays either on the surface of these elements (footprint, Fig. 28) or an any arbitrarily defined image plane, be it in cartesian or in phase space. SHADOW has a lot more features than these, this is just a short description of the features used throughout this thesis. However, in order to be able to use this code, it is necessary to know about the geometry of the spectrometer. The different parameters defining and defined by the spectrometer geometry are mutually dependent and a slight change of one of the parameters will affect all the other parameters and will possibly alter the result in an unwanted fashion. As a matter of fact, we have to think about the geometry and the parameters defining the spectrometer before actually passing them on to the SHADOW code, if we want to obtain reasonable results.

4.3   RIXS spectrometers for soft X-ray spectroscopy

RIXS spectrometers and the optical elements they are made of are placed after the target in the beamline. There are different types of XES spectrometers employing a variable number of optical elements, but they all consist of at least two elements: a grating and a detector. One of the simplest types of a XES spectrometer is the one shown in Fig. 29, basically consisting only of a grating and a detector.
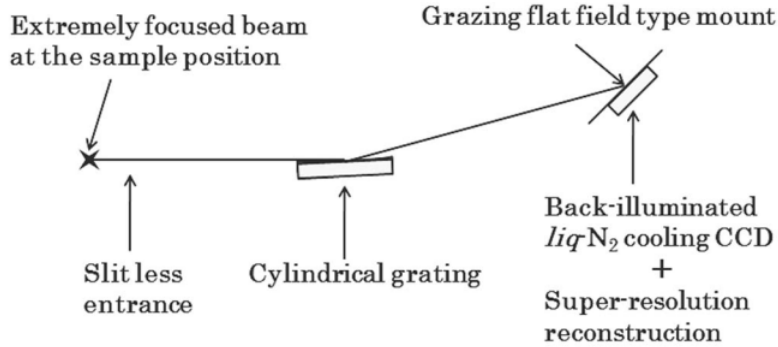
Figure 29: The schematics of a flat field type soft X-ray emission spectrometer. Shown are the main optical elements constituting the spectrometer. Taken from [11].

Photons emitted by the target at the sample position are reflected on the surface of an energy-dispersive grating and detected by a position-sensitive CCD camera. For this scheme to work, it is necessary that the beam at the sample position be extremely focused, i.e. of the order of μm or even below.

4.3.1 HORNET

The HORNET XES spectrometer is one of the three endstations of BL07LSU. As such, its optics and body are placed after the target that the X-rays are focused on by the beamline optics. It mainly consists of three optical elements: the source, i.e., the target being irradiated, the grating, and the detector 29.

- The source: One of the peculiarities of this spectrometer is its slit-less operation for increased acceptance of X-rays, requiring an extremely focused beam at the sample position (spot size of only a few μm or even less)

- The grating: The grating is a spherical variable line space (VLS) grating. Such a spherical grating has the huge advantage of reducing spherical aberrations in comparison to a plane grating. The VLS grating has the local groove density defined as

$$n(\omega) = a_0 + a_1\omega + a_2\omega^2 + a_3\omega^3 + ... \tag{32}$$

The grating in use has parameters defined up to the third order. It obeys the grating equation

$$\sin\alpha - \sin\beta = a_0 k\lambda \qquad (33)$$

In order to be able to efficiently calculate the optimal geometry for the spectrometer under the given conditions, it is necessary to define the fundamental geometry and the various parameters that are necessary for the calculation of the spectrometer energy resolution.

- The detector: a 12.5 x 12.5 mm^2 liquid-nitrogen cooled CCD camera with a pixel size of 13.5 µm^2 and a resolution of 24 µm.
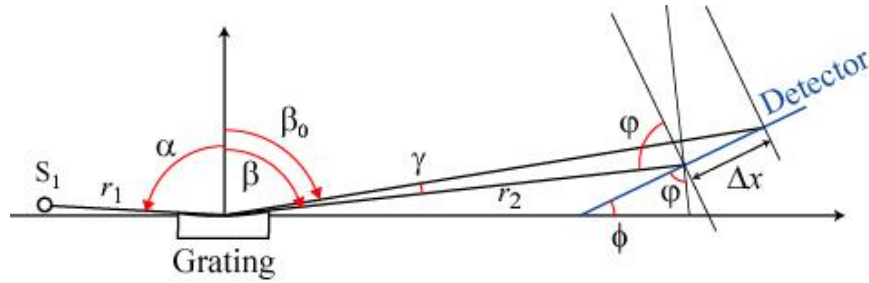

Figure 30: A flat field type soft X-ray emission spectrometer. Shown are the optical parameters that define the spectrometer geometry and thus its efficiency and its resolving power. Taken from [11].

For a more detailed discussion of the spectrometer geometry, it is necessary to define all the geometrical parameters (Fig. 30). Two rays with the same incident angle α and distinct energies E_0 and E, respectively, are reflected from the grating at angles β_0 and β. The detector plane is inclined by an angle ϕ towards the propagation direction of the central ray with energy E_0. Finally, the detector resolution Δx is the smallest distance at which two rays with reflected angles β and β' can still be distinguished from each other.

Parameter (units)					
r_1 (mm)	r_2 (mm)	α (deg)	β (deg)	Radius (mm)	Size (mm)
530.9	1969	87	83.76	16268	60 x 30
E_0 (eV)	a_0 (mm^{-1})	a_1 (mm^{-2})	a_2 (mm^{-3})	a_3 (mm^{-4})	
600	2200	$-6.031\,47 \times 10^{-1}$	$-3.117\,35 \times 10^{-3}$	$-8.993\,59 \times 10^{-6}$	

Table 1: Current parameters of the HORNET spherical VLS grating.

The parameters for the geometry as well as the VLS grating currently in use are given in Tab. 1 and the corresponding footprint for $E_0 = 600$ eV is shown in Fig. 31. The obtained footprint clearly
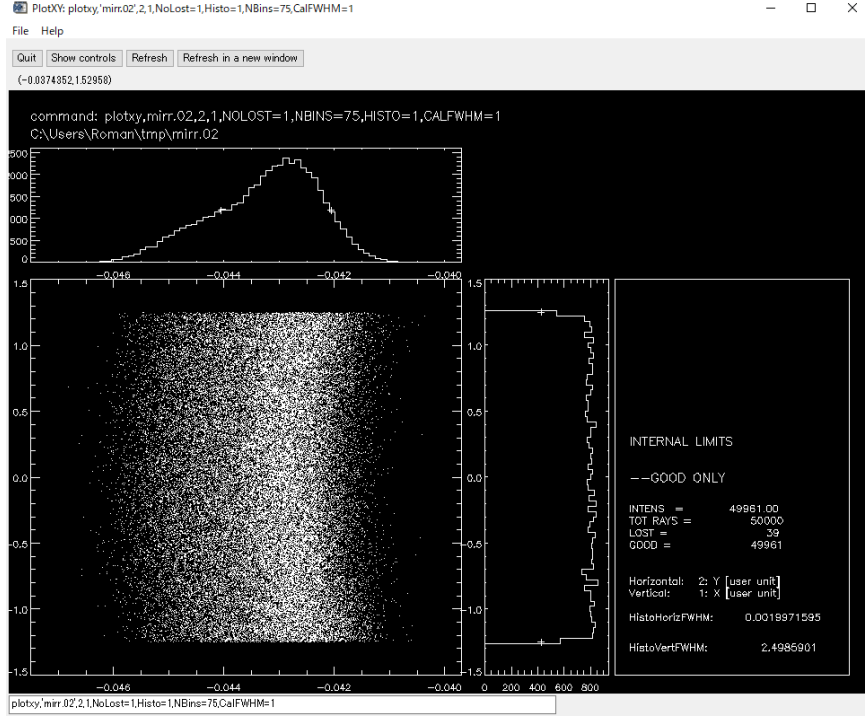
Figure 31: The footprint on the detector calculated by the SHADOW3 ray-tracing code for the current HORNET spectrometer geometry.

shows a tail to the left and as such, there are still some aberrations present, even though the grating was presumably optimised for the reference energy of $E_0 = 600\,\text{eV}$ [13].

The usability of a spectrometer is mainly defined by its resolving power and by its efficiency. The resolving power of the beamline and the spectrometer are defined as follows

$$\Delta E_S = S_1 \frac{\cos\alpha}{r_1 a_0 k\lambda} E \tag{34}$$

$$\Delta E_D = \Delta x \sin\gamma \frac{\cos\beta}{r_2 a_0 k\lambda} E, \tag{35}$$

where S_1 is size of the focused beam at the target position, and the other parameters were already defined above. For a more accurate calculation of the resolving power, one also has to take into account slope errors resulting in an imperfect grating surface. The reduction of the resolving power imposed by them is mainly dependent on the total length L of the spectrometer, and as a general rule, the longer the spectrometer, the higher the contribution of these slope errors. The contribution of the slope error is defined as

41

$$\Delta E_{SE} = \Delta_{SE} \frac{E)}{\tan[(\beta - \alpha)]/2}, \tag{36}$$

where $\Delta_S E$ is a measure of the imperfection of the grating surface and usually defined in μrad. The total or combined resolving power then is the square root of the square of the energy divergences,

$$\Delta E_{tot} = \sqrt{\Delta(E_S)^2 + \Delta(E_{SE})^2 + \Delta(E_D)^2} \tag{37}$$

Using these equations to calculate the energy resolution of HORNET, at the reference energy E_0, the resolving power of the spectrometer reaches almost $10\,000$, whereas the total resolving power without any surface errors lies at around 6000.

Whenever we are deviating from the reference energy E_0, for fixed incident angle α, we have to consider the change of the reflection angle β and either the entrance arm length r_1 or the exit arm length r_2 according to Eq. **??**. For the optimal performance, it is necessary to adjust the arm lengths depending on the incident energy E.

$$r_1 = \frac{\cos^2(\alpha)}{(\cos\alpha + \cos\beta)/R - (\cos^2(\beta))/r_1 + a_1 k\lambda}, \tag{38}$$

where R corresponds to the grating radius and $\lambda = \frac{hc}{E}$.

For fixed α and r_2, the only shifting parameters are β and r_1, leading to the resolution curve shown in Fig. 32. As is evident from this curve, the resolution drops sharply already for small deviations from the reference energy. However, this is due to insufficient optimisation and can be overcome when using a new grating with optimised design parameters.

4.4   Optimisation of the grating of HORNET spectrometer

For the current spectrometer, an update is planned, using the current spectrometer exit arm with a length of $r2 = 1969\,\mathrm{mm}$ as the primary condition for optimising the new spectrometer geometry with state-of-the-art techniques. However, the total length of the system is also limited. As shown in [25] and [26], a quite straightforward path exists for optimising a spectrometer with a spherical variable line spacing (VLS) grating.

Now, all the parameters are being defined. The geometry, that is, the entrance arm r_1 and the spectrometer length $L = r_1 + r_2$ are optimised with fixed r_2 under the condition of minimising $\Delta E_{tot} = \sqrt{\Delta(E_S)^2 + \Delta(E_{SE})^2 + \Delta(E_D)^2}$.
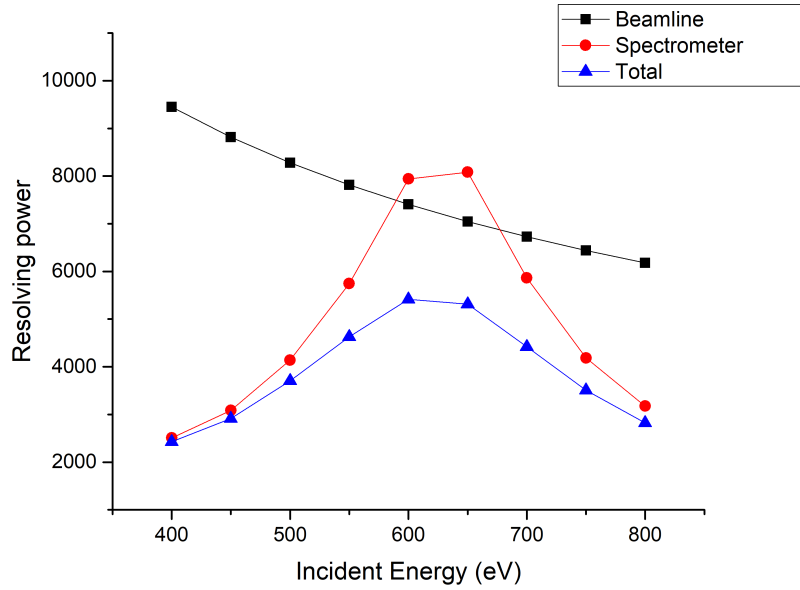
This leads to the equation

Figure 32: Resolution curve for HORNET with varying incident energy E.
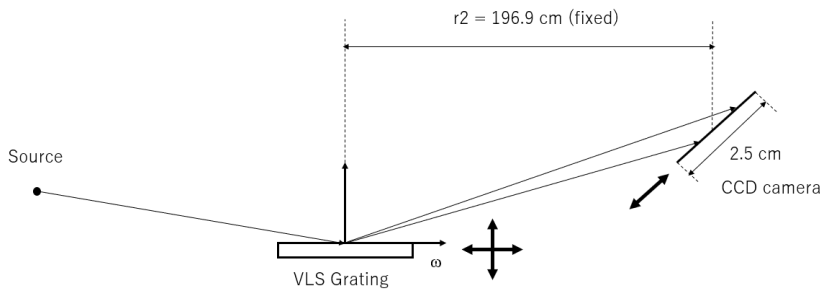

Figure 33: Sketch showing the degrees of freedom of the grating and the detector of the HORNET spectrometer arm. The conditions for the optimisation process had to be chosen so that these requirements were fulfilled.

$$L = \frac{r_2}{1 - \frac{1}{C}} \tag{39}$$

where C equals

$$C = \left(\frac{\Delta x \sin \gamma \cos \beta}{S_1 \cos \alpha} \right)^{\frac{2}{3}} \tag{40}$$

Having obtained r_1 and L, the next step is the calculation of the grating radius and the first order coefficient of the local groove density via two conditions. The first condition is that we require the system to be on focus, expressed in the equation

$$\frac{\cos^2(\alpha)}{r_1} + \frac{\cos^2(\beta)}{r_2} = \frac{\cos(\alpha) + \cos(\beta)}{R} + \frac{kK}{E_0} a_1 \tag{41}$$

and the second condition makes sure that the focal inclination curve stays tangent to the detector, giving us

$$\tan(\gamma) = \frac{\cos \beta}{2 \sin(\beta) - r_2[(\tan(\beta)/R) + a_1/a_0]} \tag{42}$$

Combining these two equations lets one first calculate the grating radius R and after that the first order coefficient of the grating expansion. The task was to find the optimal geometrical parameters for a given r_2 and predefined source size S_1 and detector resolution Δx and the subsequent calculation of all the other dependent parameters. Thus, as there are many interdependent parameters, it is not possible to change one parameter and expect an improved result, since the change of one parameter, e.g. the entrance arm length r_1, influences all the other parameters. Care needs to be taken to balance all these variables according to the given conditions. A set of source sizes $(0.5\,\mu\text{m}, 1.0\,\mu\text{m}, 1.5\,\mu\text{m}, 2.0\,\mu\text{m}, 3.0\,\mu\text{m}, 4.0\,\mu\text{m})$ and set of detector resolutions $(1\,\mu\text{m}, 2\,\mu\text{m}, 5\,\mu\text{m}, 7\,\mu\text{m}, 10\,\mu\text{m}, 13\,\mu\text{m}, 24\,\mu\text{m})$ was chosen, out of which those promising the best combined beamline plus spectrometer resolution should be the future parameters for the upgraded spectrometer. Since the operational range of HORNET usually lies within 400 to 800 eV, 600 eV was chosen as the reference energy E_0.

Having obtained the values for these parameters, one can go forward and calculate the a_2 parameter of the grating expansion in order to correct the line asymmetry. Following the derivation in [27], and setting the F_30 term corresponding to the primary coma to zero yields

$$\frac{\sin(\alpha)}{2r_1} \left(\frac{\cos^2(\alpha)}{r_1} - \frac{\cos(\alpha)}{R} \right) - \frac{\sin(\beta)}{2r_2} \left(\frac{\cos^2(\beta)}{r_2} - \frac{\cos(\beta)}{R} \right) + \frac{1}{3} a_2 k \lambda, \tag{43}$$

an analytical expression allowing the calculation of a_2 and cancellation of the coma.
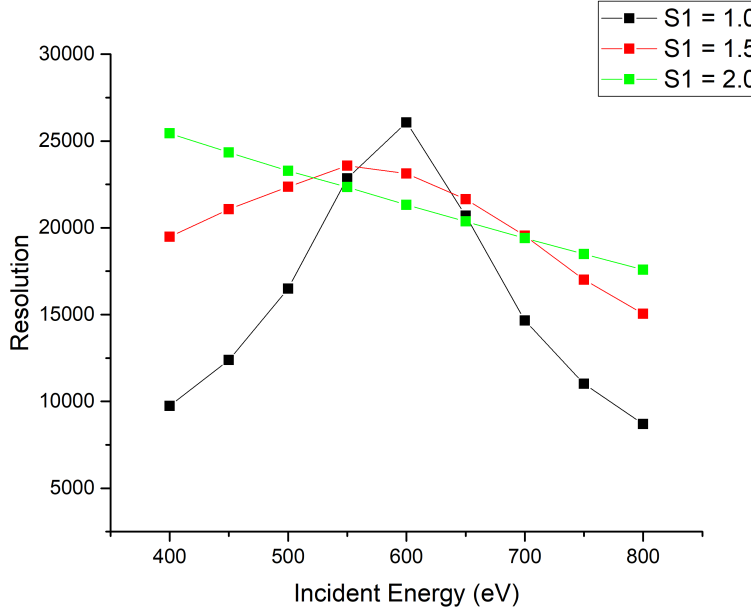
Figure 34: Resolution curve for the upgraded HORNET with varying incident energy E.

The remaining aberrations can be further reduced by calculating the a_3 coefficient of the grating expansion. However, since there is no analytical expression that allows for calculation of this parameter, one has to find a numerical solution. This was done by programming a small piece of code that uses the SHADOW code to iteratively calculate values for a_3 based on the best obtained ray-tracing results, that is, the smallest FWHM of the footprint on the detector.

The detailed results of these calculations are shown in Appendix **??**. Fig. 34 shows a comparison of the resolution curves for different source sizes for a detector resolution of $5\,\mu\text{m}$. Out of these, the most suitable configuration was picked, with a source size $S_1 = 0.5\,\mu\text{m}$ and a detector resolution $\Delta x = 5\,\mu\text{m}$.

| Parameter (units)					
r_1 (mm)	r_2 (mm)	α (deg)	β (deg)	Radius (mm)	Size (mm)
533.1	1969	87	83.76	16511	60 x 30
E_0 (eV)	a_0 (mm^{-1})	a_1 (mm^{-2})	a_2 (mm^{-3})	a_3 (mm^{-4})	
600	2200	$-6.684\,98 \times 10^{-1}$	$-2.891\,34 \times 10^{-3}$	$-8.524\,92 \times 10^{-6}$	

Table 2: Parameters for the new spherical VLS grating for the upgraded HORNET spectrometer.

Table 2 gives an overview of the parameters that are going to be used for the update of the grating for the mentioned source size and detector resolution. The corresponding beamline, spectrometer and total resolving power are 40 000, 30 000 and 20 000, respectively, which is equal to an improvement of the resolving power by a factor of 3.

Fig. **??** depicts the final plots obtained for the chosen source size and detector resolution for the energy ranging from 400 eV to 800 eV. Fig. 35a and 35b show the change of the geometric parameters of the grating and the detector, while the change in resolution depending on the energy is shown in Fig. 35c. Thus, in accordance to the graphs, if one carefully optimises the spectrometer geometry as suggested, a resolution of $\Delta E/E > 25\,000$ can be obtained over the whole energy range, which is equal to an improvement of about four times in comparison to the current spectrometer.
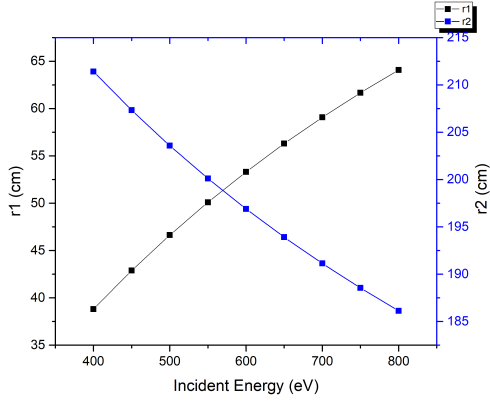
(a) Plot showing the variation of the r_1 and r_2 parameters of the spectrometer with changing incident energy.
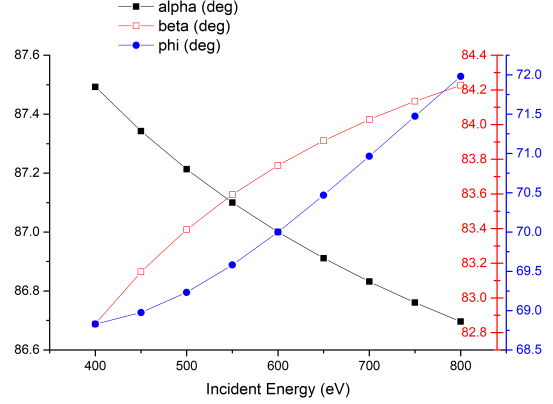
(b) Plot showing the variation of the angles α, β, and ϕ with changing incident energy.
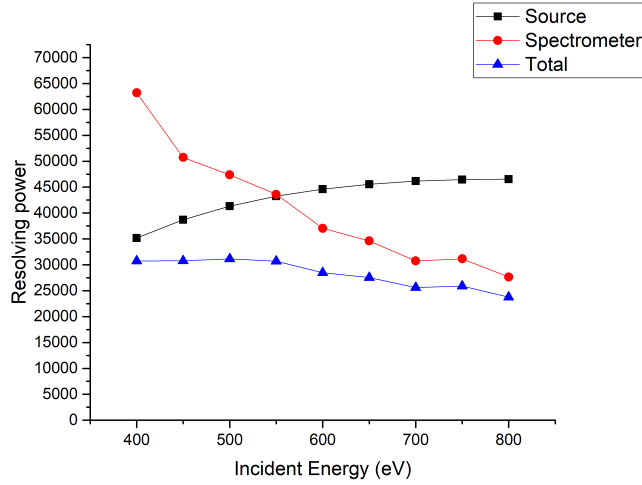
(c) Plot showing the curves for the beamline, the spectrometer, and the combined resolution over the operating energy range. Compared to Fig. 32, the resolution in general and the especially the resolution off the reference energy improved significantly.

Figure 35: Obtained specifications for the optimised spectrometer and grating for varying energy.

5   Summary

This work is a contribution to the rather new and emerging field of aqueous batteries. As explained earlier, this new technology allows for a safer use of batteries in everyday technological appliances and as such reduces the risk of overheating and explosions.

However, since the research in this field is still more or less basic and little to nothing is known about why certain mixtures work as a battery electrolyte, it is necessary to investigate the geometrical structure and the bonding network of the Li salt with water.

From earlier works, a basic understanding of the bonding network is already available, from which further investigations can start. As such, XAS and XES of Li hydrate melt with a certain mixing ratio of imide anions were measured, the result thought as an addition of the contributions of TFSI/BETI and $Li-H_2O$. To support the evidence about the structure obtained from the experiments, theoretical calculations of XES spectra of the thought building blocks of the hydrate melt were started with the aim of reproducing the experimental results. For this, a theoretical calculus was developed using the deMon2k DFT software in combination with a code using a semi-classical Kramers-Heisenberg approach for the convolution of XES spectra. Comparable methods already proved useful in the calculation of the spectra of a wide variety of different materials.

The results of these calculations were mixed. On the one hand, the theoretical spectra obtained gave useful information about the influence of the different types of molecules coordinated to the Li^+ cation on the shape of the spectrum, but on the other hand, the attempts to reproduce the overall experimental spectrum of the hydrate melt failed. Perhaps the configurations used to calculate the spectra were too much simplified and as such were not suitable as a whole to reproduce the experimental spectrum.

In order to further improve the possibilities of soft X-ray spectroscopy as a tool for investigation of the structure of water-containing liquids and other materials, a progress in spectroscopic quality is necessary. This mainly means an increase in energy resolution. Currently, all over the world new RIXS spectrometers with different concepts are under construction, reaching an energy resolution of as low as $\Delta E = 10\,\text{meV}$. However, none of these spectrometers is currently being constructed in Japan. To avoid the risk of falling behind in the development of new RIXS techniques, a new synchrotron light source called SLiT-J is scheduled for construction in 2019, and the University of Tokyo Synchrotron Radiation Research Center is planning to run a two-fold strategy for soft X-ray spectroscopy: the new beamline shall feature two RIXS spectrometers, one delivering high energy resolution and another one delivering high throughput.To aid this goal, ray-tracing calculations were performed using the popular SHADOW code, ruling out the optimal geometry and the corresponding optimised grating parameters for both spectrometers.

The results, all of them calculated with reasonable and mechanically achievable spectrometer

parameters, show a satisfying picture of the future spectrometer performance. The high-resolution spectrometer will be able to reach an energy resolution of $\Delta E = 9.3\,\text{meV}$ at the Copper L-edge at $930\,\text{eV}$ and has the capability to adapt to future detector technologies, improving the resolution even further and opening the door to new insights. For the high-throughput spectrometer, which is an updated version of the spectrometer currently in operation at SPring-8, using a new grating and a different geometry, an improvement in energy resolution of up to four times at the reference energy $E_0 = 600\,\text{eV}$, and even more off the reference energy will be achieved.

Equipped with these spectrometers, the future beamline of the University of Tokyo will become one of the leading places for the development of new RIXS techniques, and hand-in-hand with that it will enable scientists to discover new findings and new properties of materials in the soft X-ray regime.

6 Outlook

List of Figures

List of Tables

References

[1] W. Li et al. Rechargeable Lithium Batteries with Aqueous Electrolytes. *Science*, 264(5162):1115–1118, 1994. URL `http://science.sciencemag.org/content/264/5162/1115`.

[2] L. Suo et al. "Water-in-salt" electrolyte enables high-voltage aqueous lithium-ion chemistries. *Science*, 350(6263):938–943, 2015. URL `http://science.sciencemag.org/content/350/6263/938`.

[3] Y. Yamada et al. Hydrate-melt electrolytes for high-energy-density aqueous batteries. *Nature Energy*, 1:16129 EP –, Aug 2016. URL `http://dx.doi.org/10.1038/nenergy.2016.129`. Article.

[4] D. Attwood et al. *X-Rays and Extreme Ultraviolet Radiation: Principles and Applications*. Cambridge University Press, 2 edn., 2017.

[5] K.-J. Kim et al. *Synchrotron Radiation and Free-Electron Lasers: Principles of Coherent X-Ray Generation*. Cambridge University Press, 2017.

[6] T. Fransson et al. X-ray and Electron Spectroscopy of Water. *Chemical reviews*, 116 13:7551–69, 2016.

[7] T. Tokushima et al. High resolution X-ray emission spectroscopy of liquid water: The observation of two structural motifs. *Chemical Physics Letters*, 460(4):387 – 400, 2008. URL `http://www.sciencedirect.com/science/article/pii/S0009261408005745`.

[8] T. Tokushima et al. High resolution X-ray emission spectroscopy of water and its assignment based on two structural motifs. *Journal of Electron Spectroscopy and Related Phenomena*, 177(2):192 – 205, 2010. URL `http://www.sciencedirect.com/science/article/pii/S0368204810000198`. Water and Hydrogen Bonds.

[9] Y. Zhong et al. *zpch*, vol. 229, chap. Ionic Solutions Probed by Resonant Inelastic X-ray Scattering, 1855, 2018 2015. URL `https://www.degruyter.com/view/j/zpch.2015.229.issue-10-12/zpch-2015-0610/zpch-2015-0610.xml`. 10-12.

[10] J. Dvorak et al. Towards 10 meV resolution: The design of an ultrahigh resolution soft X-ray RIXS spectrometer. *Review of Scientific Instruments*, 87(11):115109, 2016. URL `https://doi.org/10.1063/1.4964847`.

[11] S. Yamamoto et al. New soft X-ray beamline BL07LSU at SPring-8. *Journal of Synchrotron Radiation*, 21(2):352–365, Mar 2014. URL `https://doi.org/10.1107/S1600577513034796`.

[12] BL07LSU OUTLINE. URL `http://www.spring8.or.jp/wkg/BL07LSU/instrument/lang-en/INS-0000001515/instrument_summary_view`.

[13] Y. Harada et al. Ultrahigh resolution soft x-ray emission spectrometer at BL07LSU in SPring-8. *Review of Scientific Instruments*, 83(1):013116, 2012. URL `https://doi.org/10.1063/1.3680559`.

[14] D. Marx et al. *Ab Initio Molecular Dynamics: Basic Theory and Advanced Methods*. Cambridge University Press, 2009.

[15] M. P. Ljungberg et al. Semiclassical description of nuclear dynamics in x-ray emission of water. *Phys. Rev. B*, 82:245115, Dec 2010. URL `https://link.aps.org/doi/10.1103/PhysRevB.82.245115`.

[16] C. Angell. A new class of molten salt mixtures the hydrated dipositive ion as an independent cation species. *Journal of the Electrochemical Society*, 112(12):1224–1227, 1960.

[17] M. P. Ljungberg et al. Core-hole-induced dynamical effects in the x-ray emission spectrum of liquid methanol. *The Journal of Chemical Physics*, 146(13):134506, 2017. URL `https://doi.org/10.1063/1.4979656`.

[18] A. A.M. Koster et al. The deMon2k Users' Guide, Version 5.0, Cinestav, Mexico-City, 2018.

[19] M. N. J.-E. R. M. B. W. Eberhardt. Coherent excitation of vibrational wave functions observed in core hole decay spectra of O2, N2 and CO. *Journal of Electron Spectroscopy and Related Phenomena*, 67, 1994.

[20] SliT-J - Synchrotron Light in Tohoku, Japan. URL `http://www.slitj.tagen.tohoku.ac.jp/index.html`.

[21] *XOP v2.4: recent developments of the x-ray optics software toolkit*, vol. 8141, 2011. URL `https://doi.org/10.1117/12.893911`.

[22] F. Cerrina et al. *"Ray Tracing of X-Ray Optical Systems" Ch. 35 in Handbook of Optics*. Mc Graw Hill, 2009.

[23] M. Sanchez del Rio et al. *SHADOW3*: a new version of the synchrotron X-ray optics modelling package. *Journal of Synchrotron Radiation*, 18(5):708–716, Sep 2011. URL `https://doi.org/10.1107/S0909049511026306`.

[24] Official repository for shadow3 (x-ray-tracer engine). URL `https://github.com/oasys-kit/shadow3`.

[25] G. Ghiringhelli et al. SAXES, a high resolution spectrometer for resonant x-ray emission in the 400–1600eV energy range. *Review of Scientific Instruments*, 77(11):113108, 2006. URL `https://doi.org/10.1063/1.2372731`.

[26] V. N. Strocov et al. Numerical optimization of spherical variable-line-spacing grating X-ray spectrometers. *J Synchrotron Radiat*, 18(Pt 2):134–142, Mar 2011. URL `http://www.ncbi.nlm.nih.gov/pmc/articles/PMC3133478/`. Ve5006[PII].

[27] A. C. Thompson et al (editors). *X-ray Data Booklet*. Lawrence Berkeley National Laboratory, University of California, 2009.

[28] N. Brookes et al. The beamline ID32 at the ESRF for soft X-ray high energy resolution resonant inelastic X-ray scattering and polarisation dependent X-ray absorption spectroscopy. *Nuclear Instruments and Methods in Physics Research Section A: Accelerators, Spectrometers, Detectors and Associated Equipment*, 903:175 – 192, 2018. URL `http://www.sciencedirect.com/science/article/pii/S0168900218308234`.